

The MOSDEF-LRIS Survey: Probing the ISM/CGM Structure of Star-forming Galaxies at $z \sim 2$ Using Rest-UV Spectroscopy

Xinnan Du (杜辛楠)¹, Alice E. Shapley², Michael W. Topping^{2,3}, Naveen A. Reddy¹, Ryan L. Sanders^{4,7}, Alison L. Coil⁵, Mariska Kriek⁶, Bahram Mobasher¹, and Brian Siana¹ Department of Physics and Astronomy, University of California, Riverside, 900 University Avenue, Riverside, CA 92521, USA; xinnan.du@ucr.edu Department of Physics and Astronomy, University of California, Los Angeles, 430 Portola Plaza, Los Angeles, CA 90095, USA Department of Astronomy/Steward Observatory, University of Arizona, 933 North Cherry Avenue, Tucson, AZ 85721, USA Department of Physics and Astronomy, University of California, Davis, One Shields Avenue, Davis, CA 95616, USA ⁵ Center for Astrophysics and Space Sciences, Department of Physics, University of California, San Diego, 9500 Gilman Drive, La Jolla, CA 92093, USA ⁶ Astronomy Department, University of California at Berkeley, Berkeley, CA 94720, USA Received 2021 March 27; revised 2021 June 20; accepted 2021 July 6; published 2021 October 20

Abstract

The complex structure of gas, metals, and dust in the interstellar and circumgalactic medium (ISM and CGM, respectively) in star-forming galaxies can be probed by Ly α emission and absorption, low-ionization interstellar (LIS) metal absorption, and dust reddening E(B-V). We present a statistical analysis of the mutual correlations among Ly α equivalent width (EW_{Ly α}), LIS equivalent width (EW_{LIS}), and E(B-V) in a sample of 157 starforming galaxies at $z \sim 2.3$. With measurements obtained from individual deep rest-UV spectra and spectral energy distribution modeling, we find that the tightest correlation exists between EW_{LIS} and E(B-V), although correlations among all three parameters are statistically significant. These results signal a direct connection between dust and metal-enriched H I gas and that they are likely cospatial. By comparing our results with the predictions of different ISM/CGM models, we favor a dusty ISM/CGM model where dust resides in H I gas clumps and Ly α photons escape through the low H I covering fraction/column density intraclump medium. Finally, we investigate the factors that potentially contribute to the intrinsic scatter in the correlations studied in this work, including metallicity, outflow kinematics, Ly α production efficiency, and slit loss. Specifically, we find evidence that scatter in the relationship between EW_{Ly α} and E(B-V) reflects the variation in the metal-to-H I covering fraction ratio as a function of metallicity and the effects of outflows on the porosity of the ISM/CGM. Future simulations incorporating star formation feedback and the radiative transfer of Ly α photons will provide key constraints on the spatial distributions of neutral hydrogen gas and dust in the ISM/CGM structure.

Unified Astronomy Thesaurus concepts: Interstellar medium (847); Galaxy spectroscopy (2171); High-redshift galaxies (734); Circumgalactic medium (1879); Extragalactic astronomy (506)

Supporting material: machine-readable table

1. Introduction

Gas, metals, and dust in the interstellar and circumgalactic medium (ISM and CGM, respectively) play a key role in the evolution of galaxies. Specifically, these components reflect the cycle of baryons through galaxies and the processes of gas accretion, star formation, chemical enrichment, and stellar feedback—which, in turn, alter the geometry and covering fraction of the ISM/CGM and determine the escape fraction of the Lyman continuum (LyC) and Ly α radiation. However, a coherent picture regarding the ISM/CGM properties of starforming galaxies has not yet been achieved, especially at high redshift. Many outstanding questions remain regarding the kinematics and spatial distributions of gas, metals, and dust. Therefore, detailed studies of the fundamental processes involving these baryonic components will enable us to gain a more comprehensive understanding of the ISM/CGM structure in star-forming galaxies and how it consequently affects the escape of radiation into the intergalactic medium (IGM) during the reionization epoch.

The rest-frame ultraviolet (UV) spectra of star-forming galaxies provide a unique perspective on the physical properties of the ISM and CGM, the latter of which is typically defined as extending to

the galaxy virial radius (Tumlinson et al. 2017). Cool, neutral hydrogen gas in the ISM/CGM is typically traced by either H I or low-ionization interstellar (LIS) absorption features, while warm/ hot ionized gas is probed by high-ionization absorption features. In addition, the strength of the LIS lines provides key information on the properties of the ISM/CGM. Unsaturated lines can be used to infer the ionic column density, while saturated lines are useful for probing outflow kinematics and estimating metal covering fractions. In terms of kinematics, due to ubiquitously observed outflows in intensely star-forming galaxies, especially at $z \gtrsim 2$, LIS absorption lines tracing foreground gas are found to be blueshifted (Pettini et al. 2001; Steidel et al. 2010; Du et al. 2018). The Ly α feature has a more complex nature. Its morphology ranges from absorption to emission (Shapley et al. 2003; Kornei et al. 2010), and the overall strength is determined by the intrinsic production of Ly α photons and the transfer through both H I gas and dust in the ISM and CGM (e.g., Trainor et al. 2019).

Empirically, Ly α and LIS equivalent widths (EW_{Ly α} and EW_{LIS}, respectively), along with dust extinction, have been used to inform the structure of the CGM. Ly α photons originate from recombination in the H II regions ionized by massive stars. As Ly α photons propagate through the ISM/ CGM, they are resonantly scattered by the intervening HI gas and absorbed by dust along their paths. Therefore, the emergent $EW_{L_{V}\alpha}$ and escape fraction place critical constraints on the

⁷ Hubble Fellow.

covering fraction of the H I gas and the distribution of dust. By examining the strength and scatter of the mutual correlations among $EW_{Ly\alpha}$, EW_{LIS} , and E(B-V), we can evaluate the relative importance of different physical processes that shape those relations and infer the key properties of the ISM/CGM in star-forming galaxies.

Metals are believed to be distributed within neutral hydrogen gas, as they are released mainly from supernova explosions. Observationally, the covering fraction of low ions (or metals that give rise to the LIS transitions) is found to be positively correlated with that of the H I gas (Reddy et al. 2016; Gazagnes et al. 2018). This result signals a direct connection between metals and the H I gas, which can naturally be explained if metal-enriched "pockets" are embedded in the H I gas. It is not yet clear, however, where dust resides in the CGM with respect to the H I gas and metals. Multiple CGM models have been proposed and tested, with different assumptions for the geometry and motion of the H I gas ("shell" versus "holes"), the distribution of dust (uniform screen versus in gas clumps), and the column density ratio of difference phases of the CGM (Neufeld 1991; Laursen et al. 2013; Duval et al. 2014; Gazagnes et al. 2018; Steidel et al. 2018).

Correlations involving $EW_{Ly\alpha}$, EW_{LIS} , and E(B-V) have been examined both in the nearby universe (e.g., Rivera-Thorsen et al. 2015; Yang et al. 2017; Jaskot et al. 2019) and at high redshift $(z \ge 2)$ using individual and composite galaxy spectra (Shapley et al. 2001, 2003; Pentericci et al. 2007, 2009; Erb et al. 2010; Berry et al. 2012; Jones et al. 2012; Hagen et al. 2014; Trainor et al. 2016; Du et al. 2018; Marchi et al. 2019; Trainor et al. 2019; Pahl et al. 2020). These previous studies have found that stronger Ly α emission is typically associated with weaker LIS lines and lower dust extinction. The codependence on Ly α further suggests a positive correlation between EW_{LIS} and E(B-V). Moreover, while $EW_{Ly\alpha}$ versus EW_{LIS} and $EW_{Ly\alpha}$ versus E(B-V) correlations appear to be redshift-independent across $z \sim 2$ –4 (Du et al. 2018), EW_{Ly\alpha} is larger at fixed EW_{LIS} and E(B-V) at $z \sim 5$ (Pahl et al. 2020), suggesting greater intrinsic Ly α production at fixed ISM/CGM properties. On the other hand, the EW_{LIS} versus E(B-V) relation does not evolve across $z \sim 2-5$ (Pahl et al. 2020), highlighting a fundamental connection between the neutral hydrogen gas and dust components in the ISM/CGM of star-forming galaxies.

The relative scatters or strengths of the correlations among $EW_{Lv\alpha}$, EW_{LIS} , and E(B-V) have also been investigated. Using composite spectra created out of nearly 1000 Lyman break galaxies (LBGs) at $z \sim 3$, Shapley et al. (2003) reported that $EW_{Ly\alpha}$ depends more strongly on EW_{LIS} than E(B-V), as suggested by a larger fractional change in EW_{LIS} across the $EW_{Lv\alpha}$ quartiles than the E(B-V) quartiles. More recently, Du et al. (2018) attempted to measure the relative scatter of these three correlations in a statistical manner. Treating composites binned according to different properties (i.e., $EW_{Lv\alpha}$, UV absolute magnitude, stellar mass, star formation rate (SFR), E(B-V), and galaxy age) as "individual" points, the authors found that EW_{LIS} and $EW_{Lv\alpha}$ are the most strongly correlated. However, the most robust method for determining the relative degree of intrinsic scatter in these relationships is based on individual measurements. Such an approach requires a significantly higher signal-to-noise ratio (S/N) for individual rest-frame UV spectra, compared to analyses based on composite spectra.

For example, Trainor et al. (2019) conducted an empirical analysis of factors affecting Ly α production and escape using a statistical sample of 703 galaxies at $z \sim 2$ –3. By characterizing

and comparing the strengths of various correlations involving $\mathrm{EW_{Ly\alpha}}$, $\mathrm{EW_{LIS}}$, galaxy properties, the ionization parameter, $\mathrm{Ly\alpha}$ kinematics, and the $\mathrm{Ly\alpha}$ escape fraction, these authors found that $\mathrm{EW_{Ly\alpha}}$ is best predicted by a linear combination of $\mathrm{EW_{LIS}}$ and [O III]/H β . However, since Trainor et al. (2019) primarily focused on the question of $\mathrm{Ly\alpha}$ production and escape, they did not directly analyze the $\mathrm{EW_{LIS}}$ versus E(B-V) relation, which can, in fact, provide additional insights into the ISM/CGM structure, as we explore in this work.

In this study, we present the first statistical analysis to characterize the nature and relative strength of the mutual correlations involving EW_{Lv α}, EW_{LIS}, and E(B-V) using rest-UV spectroscopic measurements of individual galaxies at $z \sim 2$. We further utilize available rest-optical spectra for the same galaxies to obtain supplementary measurements, such as the systemic redshift and oxygen abundance inferred from rest-optical nebular emission lines, to build a multidimensional description of each galaxy. In order to perform meaningful comparisons among the correlations, we measure $EW_{Lv\alpha}$, EW_{LIS} , and E(B-V) for all of the objects in a uniform manner. We additionally account for individual LIS nondetections to avoid potential selection biases. With a carefully constructed sample and uniform measurements, we aim to determine the most fundamental correlation among the three and infer the CGM structure and dust distribution based on our results.

This paper is organized as follows. In Section 2, we discuss the sample selection, rest-optical and rest-UV observations, redshift estimates, and sample properties. We describe the measurements in Section 3, including spectral energy distribution (SED) modeling and the EW measurements of Ly α and LIS features. We present the EW_{Ly α} and E(B-V) distributions in Section 4, along with the statistical analysis and linear regression modeling to the EW_{Ly α} versus EW_{LIS}, EW_{LIS} versus E(B-V), and EW_{Ly α} versus E(B-V) correlations. In Section 5, we discuss plausible CGM models suggested by our results and the factors contributing to the observed scatter in the correlations. We summarize the key findings in Section 6.

Throughout this paper, we adopt a standard Λ CDM model with $\Omega_m = 0.3$, $\Omega_{\Lambda} = 0.7$, and $H_0 = 70 \, \mathrm{km \, s^{-1}}$ and a solar oxygen abundance of $12 + \log(\mathrm{O/H}) = 8.69$ (Asplund et al. 2009). All wavelengths are measured in vacuum. Magnitudes and colors are on the AB system.

2. Sample and Observations

In this section, we describe the parent MOSFIRE Deep Evolution Field (MOSDEF)- Low Resolution Imager and Spectrometer (LRIS) data set, the systemic redshift determination, and the properties of the LRIS-ISM sample used in this study. For a more in-depth description of sample selection, data reduction, and redshift measurements, we refer readers to Kriek et al. (2015) and Topping et al. (2020), in which the rest-optical and rest-UV data, respectively, were first presented.

2.1. Data and Observations

2.1.1. Rest-optical MOSFIRE Spectroscopy

The MOSDEF-LRIS sample presented in this paper was drawn from the MOSDEF survey described in Kriek et al. (2015), which consists of \sim 1500 galaxies at $1.4 \le z \le 3.8$. The targets were observed on 53 multiobject slit masks using the Multi-object Spectrometer for Infrared Exploration (MOSFIRE; McLean et al. 2012) on the Keck I telescope between 2012 and 2016.

Rest-frame optical spectra were obtained with the Y, J, H, and K filters, which optimize the coverage of strong rest-optical emission lines ([O II] $\lambda\lambda$ 3727, 3729, H β , [O III] $\lambda\lambda$ 4959, 5007, H α , [N II] λ 6584, and [S II] $\lambda\lambda$ 6717, 6731) for objects in the redshift windows $1.37 \le z \le 1.70$, $2.09 \le z \le 2.61$, and $2.95 \le z \le 3.80$.

The targets were H-band selected and have an approximate corresponding lower stellar-mass limit of $\sim 10^9~M_\odot$ in each redshift bin. The MOSDEF targets are located in extragalactic legacy fields covered by the CANDELS (Grogin et al. 2011; Koekemoer et al. 2011) and 3D-HST surveys (Brammer et al. 2012), where extensive spectroscopic and multiwavelength photometric data are publicly available and enable a multi-dimensional view of each galaxy. The MOSFIRE spectra were reduced, optimally extracted, and placed on an absolute flux scale as described in Kriek et al. (2015).

2.1.2. Rest-UV LRIS Spectroscopy

A detailed description of the rest-UV sample selection, data collection, and data reduction is provided in Topping et al. (2020), and here we only provide an overview. In summary, a subset of MOSDEF galaxies were selected for rest-UV spectroscopic follow-up using LRIS (Oke et al. 1995; Steidel et al. 2004) on the Keck I telescope. The follow-up observations prioritized targets with individually detected strong rest-optical lines (H β , [O III], $H\alpha$, and [N II]). We also included MOSDEF galaxies with confirmed spectroscopic redshifts and objects from the 3D-HST catalog with similar photometric redshifts and apparent magnitudes to those of the MOSDEF galaxies. A total of 260 galaxies were observed within the redshift ranges of $1.40 \le z \le 1.90$, $1.90 \le z \le 2.65$, and $2.95 \le z \le 3.80$. The vast majority of MOSDEF-LRIS galaxies (215 out of 260) have spectroscopic redshift measurements inferred from rest-optical nebular emission lines in the MOSFIRE spectra. Of the remaining 45 objects (hereafter the "LRIS-only" galaxies), 21 have a redshift estimated based on rest-UV emission and absorption features (see Section 2.2). The remaining 24 LRIS-only galaxies do not have robust redshift measurements.

Multislit rest-UV spectroscopy was obtained using Keck/ LRIS, a dichroic spectrograph, in the COSMOS, AEGIS, GOODS-N, and GOODS-S fields over the course of 10 nights in 2017 and 2018. The LRIS data were collected on nine multiobject slit masks with 1"2 slits. All masks were observed with the 400 lines mm⁻¹ grism blazed at 3400 Å on the blue side (435 km s_.⁻¹ FWHM) and the 600 lines mm⁻¹ grating blazed at 5000 Å on the red side (220 km s⁻¹ FWHM). This configuration enabled continuous wavelength coverage from 3100 to \sim 7650 Å in the observed frame, covering a number of strong rest-UV spectral lines given the redshift ranges probed. These include Ly α ; low-ionization Si II λ 1260, O I λ 1302+Si II λ 1304, C II λ 1334, Si II λ 1526, Fe II λ 1608, and Al II λ 1670 absorption features; high-ionization Si IV $\lambda\lambda$ 1393, 1402 and C IV $\lambda\lambda$ 1548, 1550 absorption features; and O III] $\lambda\lambda$ 1661, 1665, He II λ 1640, and C III] $\lambda\lambda$ 1907, 1909 emission features. The integration time ranged from 6 to 11 hr for different masks, with a median of \sim 7.5 hr. Observing conditions were fair, yielding a moderate (average 0.18) seeing.

The data were reduced using customized IRAF, IDL, and Python scripts as described in Topping et al. (2020). In brief, the two-dimensional (2D) spectra were rectified, flat-fielded, cut up into individual slitlets, cleaned of cosmic rays, background-subtracted, and median-stacked. The relative order of the last three steps listed above was slightly different for the

blue- and red-side slitlets to optimize the data quality, given that the red side is more heavily affected by cosmic rays (see Topping et al. 2020, for details). To avoid overestimation of the background due to the presence of the target (Shapley et al. 2006), a second-pass background subtraction was performed for each object, during which the trace determined from the stacked 2D spectrum was masked out. Afterward, the 2D spectra were extracted into one dimension (1D) and wavelength- and flux-calibrated. The flux calibration included two steps, a relative calibration using a spectrophotometric standard star and an absolute calibration to scale our spectrophotometric measurements to those listed in the 3D-HST photometric catalog. Finally, additional continuum correction was applied to a small number of objects to ensure the consistency of the continuum levels on either side of the dichroic at ~5000 Å.

2.2. Redshift Measurements

For most (215 out of 260) objects in the MOSDEF-LRIS sample, the systemic redshift was robustly measured using the rest-optical emission lines (H β , [O III], H α , [N II], and [S II]), with the initial guess derived from the highest-S/N emission line, typically H α or [O III] λ 5007 (Kriek et al. 2015). For 21 out of 45 LRIS-only objects, with no previous MOSFIRE redshift, a systemic redshift measurement was obtained based on Ly α emission and/or LIS absorption lines (Si II λ 1260, O I λ 1302+Si II λ 1304, C II λ 1334, Si II λ 1526, Fe II λ 1608, and Al II λ 1670), as described in detail in Topping et al. (2020). A variety of velocity rules were applied to the Ly α - and LISbased redshifts ($z_{Ly\alpha}$ and z_{LIS} , respectively) in order to account for the presence of galaxy-scale outflows. The z_{LIS} was used to calculate the systemic redshift whenever available and assumed to have a blueshift of -32 and $-89 \,\mathrm{km \, s^{-1}}$, respectively, for objects with only z_{LIS} (eight galaxies) and both z_{LIS} and $z_{Ly\alpha}$ measurements (five galaxies). In cases where only $z_{Lv\alpha}$ was available, Ly α was assumed to have a redshift of +153 and $+317 \,\mathrm{km \, s^{-1}}$ for objects at $z \le 2.7$ (seven galaxies) and z > 2.7(one galaxy), respectively. All of the observed-frame spectra were then shifted into the rest frame according to the systemic redshift determined using the methods above.

2.3. Sample

In this study, we aim to examine the mutual correlations among $EW_{Ly\alpha}$, EW_{LIS} , and dust reddening E(B-V). For this purpose, we selected a subsample of galaxies that have simultaneous coverage of Ly α , Si II λ 1260, O I λ 1302+Si II λ 1304, and C II λ 1334, which corresponds to the rest-frame wavelength range of 1208–1344 Å. In order to retain a sufficiently large sample, we did not further require the coverage of the redder LIS lines, namely, Si II $\lambda 1526$, Fe II $\lambda 1608$, and Al II $\lambda 1670$. Calculating EW_{LIS} based on Si II $\lambda 1260$, O I+Si II, and C II additionally enables a direct comparison with the results presented in Du et al. (2018), where the relations among $EW_{Lv\alpha}$, EW_{LIS} , and E(B-V) were examined in stacked spectra with the LIS EW measured from the same three features. The spectral coverage requirement excludes 15 objects from the sample. Moreover, to avoid potential redshift evolution in the relations of interest, we only included objects with a systemic redshift $z \leq 2.7$, which is consistent with the redshift boundary chosen for the $z\sim 2$ sample presented in Du et al. (2018). With this redshift threshold, all of the relevant lines (Ly α and three LIS lines) fall on the blue side of the spectrum. Twentytwo z > 2.7 galaxies were removed from the sample according to

this criterion. We also imposed a few more criteria to exclude objects for which the spectra are subject to nearby contamination and/or artifacts (27 galaxies) and those identified as active galactic nuclei (13 galaxies) based on X-ray luminosities, Spitzer/IRAC colors, or [N II] $\lambda6584/H\alpha$ ratios (Coil et al. 2015; Azadi et al. 2017, 2018; Leung et al. 2019). Finally, we removed two objects with anomalously large error bars on their $EW_{Ly\alpha}$ measurements: COSMOS-4029 ($EW_{Ly\alpha}=21.9\pm296.0$ Å) and GOODS-N-29834 ($EW_{Ly\alpha}=195.3\pm1125.0$ Å). These two galaxies both have a close-to-zero red-side continuum (1225–1255 Å; see Section 3.2.1 for details of the $Ly\alpha$ EW measurement) and a noise level comparable to the continuum. Therefore, the exclusion of these two objects from the final sample was based on the fact that we were unable to obtain meaningful measurements of $EW_{Ly\alpha}$ for them.

In the end, the selected subsample (hereafter the "LRIS-ISM" sample) consists of 157 galaxies, of which 16 are LRIS-only objects. We summarize the galaxy properties and line measurements of the LRIS-ISM objects in Table 1 and plot the overall rest-UV composite spectrum in the wavelength range of interest in Figure 1. As shown in Figure 2 and the bottom panel of Figure 3, our LRIS-ISM sample has a redshift range of $1.65 \le z \le 2.58$ with a median of 2.27, a stellar-mass range of $8.64 < \log (M_*/M_\odot) < 11.14$ with a median of 9.94, an SFR range of $2 \le (\text{SFR}/M_\odot \text{ yr}^{-1}) \le 336$ with a median of $15 \ M_\odot \ \text{yr}^{-1}$, and dust reddening range of 0.01 < E(B-V) < 0.435 with a median of 0.10. We describe the SED modeling in Section 3.1.

3. Measurements

One unique aspect of our study is the ability to characterize the relative tightness of the relations among $\mathrm{EW}_{\mathrm{Ly}\alpha}$, $\mathrm{EW}_{\mathrm{LIS}}$, and E(B-V) using measurements from individual galaxies in order to gain insight into the distribution of gas and dust in distant star-forming galaxies. In this section, we describe the SED modeling for obtaining dust reddening and other stellar population parameters (Section 3.1), as well as the measurements of the rest-frame $\mathrm{Ly}\alpha$ EW (Section 3.2.1) and the total EW of multiple LIS features (Section 3.2.2).

3.1. SED Modeling

We inferred the key parameters (such as dust reddening, stellar mass, age, and SFR) of individual galaxies in the LRIS-ISM sample by modeling their broadband photometry, as cataloged by the 3D-HST survey (Skelton et al. 2014). When applicable, the photometry was corrected for rest-optical ([O II], $H\beta$, [O III], $H\alpha$, and [N II]) and $Ly\alpha$ line emission prior to the fitting.

Galaxy SEDs were fit with stellar population templates from Bruzual & Charlot (2003) assuming a Chabrier (2003) initial mass function (IMF). Following Reddy et al. (2018) and Du et al. (2018), we modeled each galaxy with two different combinations of metallicity and extinction curves: 1.4 solar metallicity ($Z_{\odot}=0.014$) with the Calzetti et al. (2000) attenuation curve (hereafter "1.4 Z_{\odot} +Calzetti") and 0.28 Z_{\odot} with the small magellanic cloud (SMC) extinction curve (hereafter "0.28 Z_{\odot} +SMC"). Although each model grid included different star formation histories (exponentially declining, constant, and rising) and wide ranges in age and dust reddening, we chose to adopt the constant SFR model, as it is proven to be a satisfactory description of the star formation history for the typical star-forming galaxies at $z \sim 2$ (Reddy et al. 2012; Steidel et al. 2014; Strom et al. 2017).

We set a lower age limit of 50 Myr, provided the typical dynamical timescales of $z \sim 2$ galaxies (Reddy et al. 2012), and an upper age limit of the age of the universe at the redshift of each galaxy. We also considered stellar continuum reddening in the range 0.0 < E(B-V) < 0.6.

Recent work suggests that subsolar-metallicity models with an SMC curve provide a better description for low- and moderate-mass star-forming galaxies at $z\gtrsim 2$ than the traditionally assumed combination of solar metallicity and a Calzetti et al. (2000) curve based on the IRX- β relation (e.g., Reddy et al. 2018) and the overall fit to the galaxy SEDs (Du et al. 2018). As a result, we adopted the 0.28 Z_{\odot} +SMC model for the LRIS-ISM galaxies with log $(M_*/M_{\odot}) < 10.04$ and the 1.4 Z_{\odot} +Calzetti model for those with log $(M_*/M_{\odot}) \geqslant 10.04$, where log (M_*/M_{\odot}) was estimated based on the 1.4 Z_{\odot} +Calzetti model. This stellar-mass threshold corresponds to nebular dust reddening $E(B-V)_{\rm neb}=0.3$, according to the $E(B-V)_{\rm neb}$ versus M_* relation in Shivaei et al. (2020), and we estimated $E(B-V)_{\rm neb}$ for each galaxy based on the Balmer decrement assuming a Cardelli et al. (1989) law.

To obtain the best-fit stellar population parameters and their uncertainties, we created 100 realizations of the SED for each galaxy by perturbing its photometric measurements with the associated 1σ errors listed in the 3D-HST photometric catalog. The same modeling described above was performed on these 100 realizations, resulting in 100 sets of best-fit parameters for each object determined by the minimum χ^2 method. The median value and standard deviation of those 100 measurements were adopted as the best-fit stellar population parameter and 1σ uncertainty, respectively.

3.2. Line Measurements

3.2.1. Lyα

We measured the rest-frame $Ly\alpha$ EW following the procedures described in Kornei et al. (2010) and Du et al. (2018). The spectral morphology of $Ly\alpha$ in individual galaxy spectra was classified into four categories through visual inspection: "emission", "absorption", "combination", and "noise". "Emission" objects show dominant $Ly\alpha$ emission on top of a relatively flat continuum, while the $Ly\alpha$ emission for "combination" objects is superimposed on a large absorption trough. The $Ly\alpha$ morphology is classified as "absorption" when a broad absorption trough resides around the rest-frame wavelength of $Ly\alpha$ and "noise" when the spectrum is featureless near $Ly\alpha$.

Galaxies in the LRIS-ISM sample were mainly categorized as "combination" (61 galaxies), "absorption" (48 galaxies), and "noise" objects (38 galaxies), with only a small fraction identified as "emission" objects (10 galaxies). For each object, regardless of their spectral morphology, the blue- and red-side continuum levels were estimated over wavelength ranges of 1120-1180 and 1225-1255 Å, respectively. For "emission", "combination", and "absorption" objects, the Ly α flux was integrated between the blue and red wavelength "boundaries," where the flux density level on either side of the Ly α feature (either emission or absorption) first meets the blue- and red-side continuum level, respectively. The blue boundary was fixed at 1208 Å for the "emission" objects and forced to be no bluer than 1208 Å for the "combination" objects (Du et al. 2018). For the "noise" objects, the $Ly\alpha$ flux was integrated over 1199.9-1228.8 Å, the boundaries adopted in Kornei et al. (2010). Finally, we computed the Ly α EW by dividing the enclosed Ly α flux by the red-side continuum flux

Table 1
Galaxy Properties and Line Measurements

Field	ID	Redshift	E(B-V)	$\mathrm{EW}_{\mathrm{Ly}lpha} \ (\mathrm{\mathring{A}})$	EW _{LIS} (Å)	LIS Category
AEGIS	3668	2.1877	0.110 ± 0.011	0.6 ± 0.6	-9.7 ± 0.4	D
AEGIS	4711	2.1836	0.010 ± 0.007	26.2 ± 0.7	-3.5 ± 0.8	P
AEGIS	6311	2.1878	0.200 ± 0.008	-4.3 ± 1.2	-9.2 ± 1.1	D
AEGIS	6569	2.0857	0.080 ± 0.008	7.9 ± 5.2	-6.0 ± 1.7	C
AEGIS	10471	2.3736	0.330 ± 0.011	-15.7 ± 4.7	>-11.0	L
AEGIS	10494	2.2963	0.435 ± 0.007	-19.4 ± 3.0	-5.7 ± 1.4	C
AEGIS	12918	2.4348	0.100 ± 0.008	-8.1 ± 6.4	-10.7 ± 3.2	P
AEGIS	14957	2.3013	0.080 ± 0.008	-10.2 ± 2.4	-10.1 ± 2.5	C
AEGIS	16496	2.1694	0.260 ± 0.007	18.2 ± 4.0	-14.2 ± 5.0	P
AEGIS	18543	2.1387	0.030 ± 0.008	1.5 ± 0.8	-5.9 ± 0.4	D
AEGIS	20924	2.2650	0.310 ± 0.014	18.1 ± 24.6	-9.1 ± 0.4	D
AEGIS	21675	2.4631	0.190 ± 0.014	-9.1 ± 2.2	>-5.8	L
AEGIS	22931	2.2952	0.050 ± 0.007	9.9 ± 0.4	-5.0 ± 0.5	D
AEGIS	23409	2.2946	0.090 ± 0.008	-3.0 ± 0.9	-7.7 ± 1.7	P
AEGIS	24481	2.1334	0.240 ± 0.012	-10.3 ± 1.2	-11.3 ± 2.9	P
AEGIS	25522	2.2295	0.120 ± 0.009	-25.8 ± 2.3	-8.9 ± 0.8	D
AEGIS	25817	2.2870	0.070 ± 0.007	-23.0 ± 3.6	-10.1 ± 0.7	D P
AEGIS	27627	1.6742	0.150 ± 0.006	-15.5 ± 3.4	-9.1 ± 2.7	P P
AEGIS	27825	2.2926	0.340 ± 0.014	-10.2 ± 2.4	-11.5 ± 2.9	P P
AEGIS	28421	2.2928	0.370 ± 0.007	-17.6 ± 4.9 -19.6 ± 2.5	-12.9 ± 2.9	P D
AEGIS	28659	2.3120	0.250 ± 0.010		-9.4 ± 1.5	L L
AEGIS AEGIS	28710 29650	2.1851 2.2684	0.215 ± 0.016	-7.9 ± 4.7	>-10.7 -8.1 ± 0.8	D D
AEGIS AEGIS	30074	2.2113	$0.220 \pm 0.011 \\ 0.310 \pm 0.010$	25.0 ± 2.2 -7.0 ± 1.3	-8.1 ± 0.8 -9.2 ± 1.9	D P
AEGIS AEGIS	30278	2.2003	0.310 ± 0.010 0.230 ± 0.014	-7.0 ± 1.3 13.2 ± 18.6	-9.2 ± 1.9 >-7.0	L L
AEGIS AEGIS	32354	2.1328	0.230 ± 0.014 0.090 ± 0.013	3.0 ± 1.1	-7.7 ± 0.7	D
AEGIS	32638	2.4080	0.090 ± 0.013 0.120 ± 0.013	0.7 ± 0.8	-7.7 ± 0.7 -8.7 ± 0.7	D
AEGIS	33768	2.3248	0.120 ± 0.013 0.390 ± 0.046	0.7 ± 0.8 0.3 ± 3.6	-8.7 ± 0.7 -9.9 ± 2.7	P
AEGIS	33808	2.2254	0.390 ± 0.040 0.140 ± 0.007	-13.0 ± 1.1	-9.9 ± 2.7 -9.0 ± 1.8	P
AEGIS	33942	2.1608	0.090 ± 0.009	-13.0 ± 1.1 1.7 ± 1.5	-5.3 ± 0.8	D
AEGIS	34661	2.1320	0.090 ± 0.006 0.090 ± 0.006	-23.7 ± 3.1	-3.3 ± 0.8 -11.7 ± 1.2	D
AEGIS	34813	2.2328	0.070 ± 0.000 0.070 ± 0.007	-23.7 ± 3.1 -16.9 ± 2.4	-8.6 ± 1.2	D
AEGIS	36257	2.1307	0.070 ± 0.007 0.170 ± 0.010	-10.0 ± 1.8	-9.2 ± 2.0	P
AEGIS	36451	2.1334	0.390 ± 0.024	71.1 ± 2.8	>-10.9	L
AEGIS	40851	2.2672	0.010 ± 0.009	6.0 ± 1.2	-7.3 ± 0.8	D
COSMOS	241	2.3131	0.030 ± 0.007	1.4 ± 0.9	-4.5 ± 1.1	C
COSMOS	541	2.0810	0.060 ± 0.006	24.6 ± 2.4	-5.2 ± 1.9	P
COSMOS	964	2.2903	0.080 ± 0.006	-13.3 ± 4.9	-12.9 ± 3.6	P
COSMOS	2207	2.0976	0.060 ± 0.007	12.7 ± 2.7	>-5.8	L
COSMOS	2672	2.3074	0.230 ± 0.010	48.3 ± 12.0	>-11.1	L
COSMOS	2786	2.2980	0.120 ± 0.008	-16.1 ± 4.9	>-6.9	L
COSMOS	3112	2.3080	0.220 ± 0.009	-12.2 ± 1.9	-9.3 ± 2.5	P
COSMOS	3185	2.1732	0.090 ± 0.007	-17.8 ± 3.9	-8.2 ± 2.6	P
COSMOS	3324	2.3072	0.280 ± 0.009	-9.5 ± 3.5	-14.7 ± 3.5	P
COSMOS	3626	2.3247	0.040 ± 0.004	-13.7 ± 0.3	-5.6 ± 0.4	D
COSMOS	3666	2.0859	0.310 ± 0.007	-4.1 ± 1.2	-4.2 ± 1.2	P
COSMOS	3974	2.0979	0.230 ± 0.005	78.0 ± 7.3	>-8.7	L
COSMOS	4078	2.4409	0.080 ± 0.005	-20.1 ± 6.2	-15.4 ± 4.7	P
COSMOS	4156	2.1898	0.040 ± 0.007	21.7 ± 1.9	-7.2 ± 1.9	P
COSMOS	4441	2.2243	0.050 ± 0.006	-0.7 ± 3.8	-5.1 ± 1.6	C
COSMOS	4446	2.1970	0.080 ± 0.005	8.7 ± 0.9	-5.8 ± 1.4	P
COSMOS	4497	2.4413	0.250 ± 0.009	-18.2 ± 5.3	-11.9 ± 2.3	P
COSMOS	4930	2.2265	0.300 ± 0.010	-9.0 ± 4.5	-9.2 ± 2.4	P
COSMOS	4945	2.0813	0.050 ± 0.009	2.5 ± 1.1	>-3.9	L
COSMOS	4962	2.1725	0.050 ± 0.007	-6.5 ± 3.6	>-7.3	L
COSMOS	5107	2.1443	0.200 ± 0.009	-12.1 ± 3.5	-6.1 ± 1.7	P
COSMOS	5462	2.5221	0.270 ± 0.007	-16.0 ± 4.2	-8.0 ± 2.6	C
COSMOS	5571	2.2779	0.240 ± 0.010	-4.8 ± 0.8	-5.3 ± 0.8	D
COSMOS	5686	2.0956	0.260 ± 0.011	-7.1 ± 1.6	-8.1 ± 2.9	P
COSMOS	5814	2.1266	0.290 ± 0.008	-7.0 ± 1.7	-7.6 ± 1.0	D
COSMOS	5901	2.3962	0.200 ± 0.012	-18.8 ± 1.6	-9.6 ± 2.0	P
COSMOS	6179	1.8506	0.420 ± 0.006	-12.1 ± 5.6	-15.8 ± 5.2	P
COSMOS	6283	2.2238	0.070 ± 0.005	-28.7 ± 2.0	-8.6 ± 0.9	D

Table 1 (Continued)

Field ID Redshift $E(B-V)$ EW_{LVG} EW_{LIS} LIS 0						
Field	ID	Reasnitt	E(B-V)	$rac{\mathrm{EW_{Lylpha}}}{\mathrm{(A)}}$	EW _{LIS} (Å)	LIS Category
COSMOS	6379	2.4382	0.090 ± 0.006	9.8 ± 2.2	>-3.4	L
COSMOS	6417	2.0998	0.070 ± 0.007	-22.0 ± 2.6	-5.5 ± 1.3	P
COSMOS	6817	2.0944	0.110 ± 0.009	-11.1 ± 3.6	>-5.1	L
COSMOS	6826	2.4351	0.200 ± 0.010	3.3 ± 4.7	>-7.7	L
COSMOS COSMOS	6963 7430	2.3014 1.9248	0.340 ± 0.004	22.3 ± 2.5 -15.0 ± 9.2	>-5.9 >-7.9	L L
COSMOS	7430 7735	2.4399	0.100 ± 0.006 0.100 ± 0.005	-13.0 ± 9.2 -3.2 ± 1.2	>-7.9 -7.3 ± 0.8	D D
COSMOS	7883	2.1529	0.060 ± 0.005	-3.2 ± 1.2 18.4 ± 1.2	-7.5 ± 0.8 -7.6 ± 2.8	P
COSMOS	8081	2.1633	0.070 ± 0.008	-39.1 ± 10.9	>-6.0	L
COSMOS	8515	2.4537	0.060 ± 0.003	6.0 ± 1.2	-4.2 ± 0.6	D
COSMOS	8540	2.0912	0.060 ± 0.007	-15.9 ± 2.1	-6.1 ± 1.6	C
COSMOS	9044	2.1988	0.150 ± 0.009	-15.4 ± 1.8	-9.3 ± 1.1	D
COSMOS	9251	2.2426	0.050 ± 0.009	28.6 ± 4.8	-8.6 ± 3.0	C
COSMOS	10066	2.4133	0.090 ± 0.005	5.7 ± 2.1	-12.8 ± 4.1	P
COSMOS	10143	2.3776	0.060 ± 0.004	14.7 ± 0.7	-4.5 ± 1.0	P
COSMOS	10235	2.0999	0.200 ± 0.008	-17.6 ± 8.1	-9.2 ± 2.4	P
COSMOS	10280	2.1945	0.060 ± 0.005	-8.2 ± 1.5	-5.1 ± 0.6	D
COSMOS	10835	2.4139	0.100 ± 0.005	25.7 ± 19.8	>-13.9	L
COSMOS	11443	2.4561	0.080 ± 0.006	0.8 ± 2.1	-11.3 ± 3.6	P
COSMOS	11530	2.0969	0.030 ± 0.009	57.2 ± 1.4	-2.5 ± 0.3	D
COSMOS	12577	2.5365	0.350 ± 0.004	-22.2 ± 1.7	-10.8 ± 3.8	P
COSMOS	13101	1.9727	0.200 ± 0.006	-6.2 ± 3.5	>-11.6	L
COSMOS	13299	2.3089	0.310 ± 0.009	-39.1 ± 17.3	>-9.8	L
COSMOS	13364	2.1508	0.060 ± 0.006	10.9 ± 1.5	-11.2 ± 3.7	P
COSMOS	16545	2.2750	0.070 ± 0.005	-4.3 ± 0.9	-6.9 ± 0.4	D D
COSMOS COSMOS	19439 19712	2.4663 2.4863	0.210 ± 0.013	13.0 ± 2.1 -17.1 ± 5.8	-9.1 ± 1.2 >-28.5	L L
COSMOS	19712	2.1882	0.350 ± 0.014 0.270 ± 0.011	-17.1 ± 3.8 -47.3 ± 1.7	-28.3 -12.0 ± 0.5	D D
COSMOS	20062	2.1857	0.270 ± 0.011 0.260 ± 0.011	-47.3 ± 1.7 -3.9 ± 0.5	-12.0 ± 0.5 -11.2 ± 0.6	D D
COSMOS	21780	2.4718	0.260 ± 0.011 0.060 ± 0.005	-3.3 ± 0.3 -10.3 ± 0.8	-5.8 ± 0.9	D
COSMOS	21955	2.4676	0.230 ± 0.012	-22.2 ± 5.2	-13.8 ± 4.0	P
COSMOS	24020	2.0923	0.080 ± 0.006	10.7 ± 2.3	-6.9 ± 2.4	P
COSMOS	25322	2.5188	0.050 ± 0.005	7.8 ± 0.8	-6.7 ± 1.4	P
COSMOS	26073	2.2235	0.350 ± 0.015	21.2 ± 12.3	>-46.5	L
COSMOS	27120	2.4784	0.160 ± 0.006	-1.9 ± 0.6	-6.6 ± 0.7	D
COSMOS	27216	2.4225	0.030 ± 0.005	25.9 ± 3.4	-10.0 ± 2.8	P
COSMOS	27906	2.1961	0.050 ± 0.005	-7.5 ± 2.0	-6.0 ± 1.2	P
COSMOS	28258	2.4732	0.205 ± 0.010	-20.1 ± 5.2	-9.7 ± 3.0	P
GOODS-N	10596	2.2135	0.150 ± 0.009	-4.7 ± 0.6	-7.6 ± 0.7	D
GOODS-N	10645	2.1796	0.190 ± 0.010	-13.0 ± 5.3	-13.6 ± 1.5	D
GOODS-N	12157	2.2765	0.195 ± 0.020	-2.8 ± 2.3	-10.6 ± 1.3	D
GOODS-N	12345	2.2721	0.220 ± 0.010	-9.8 ± 2.6	-9.9 ± 0.5	D
GOODS-N	12980	2.2697	0.090 ± 0.006	-20.4 ± 5.2	-8.2 ± 2.3	P
GOODS N	15186	2.4139	0.090 ± 0.010	-44.2 ± 30.0	>-10.7	L
GOODS N	16351	1.6511	0.060 ± 0.007	24.0 ± 3.8	>-5.7	L
GOODS-N GOODS-N	17530 17714	2.2064 2.2349	0.100 ± 0.006 0.070 ± 0.006	15.0 ± 1.3 -17.7 ± 2.2	>-1.8 -7.2 ± 1.4	L P
GOODS-N	19067	2.2829	0.070 ± 0.000 0.070 ± 0.006	-17.7 ± 2.2 -3.8 ± 1.2	-7.2 ± 1.4 -8.2 ± 2.4	P
GOODS-N	19350	2.2367	0.070 ± 0.008 0.070 ± 0.008	-3.8 ± 1.2 -18.8 ± 1.7	-6.2 ± 2.4 -6.7 ± 1.0	D
GOODS-N	19654	2.5519	0.060 ± 0.003	-6.0 ± 1.7	-0.7 ± 1.0 -15.1 ± 5.3	P
GOODS-N	20924	2.5511	0.150 ± 0.008	-20.1 ± 1.9	>-15.7	L
GOODS-N	21279	2.4197	0.360 ± 0.010	-38.6 ± 5.8	>-8.6	L
GOODS-N	21617	2.2062	0.200 ± 0.009	1.7 ± 0.6	-5.7 ± 0.5	D
GOODS-N	21845	2.5509	0.190 ± 0.009	-2.1 ± 1.1	-6.1 ± 1.6	P
GOODS-N	22235	2.4298	0.070 ± 0.005	-1.6 ± 1.2	-6.4 ± 0.5	D
GOODS-N	22487	2.4205	0.310 ± 0.010	-13.8 ± 5.2	-6.9 ± 2.1	C
GOODS-N	22669	2.1340	0.140 ± 0.011	-13.4 ± 0.9	-6.5 ± 0.6	D
GOODS-N	23344	2.4839	0.370 ± 0.026	-23.5 ± 6.9	-8.5 ± 3.1	P
GOODS-N	23869	2.2438	0.290 ± 0.011	-28.6 ± 6.6	>-6.7	L
GOODS-N	24328	2.4072	0.070 ± 0.005	-32.9 ± 0.8	-7.5 ± 0.5	D
GOODS-N	24825	2.3347	0.060 ± 0.005	-4.1 ± 1.7	>-2.8	L
GOODS-N	24846	2.1872	0.040 ± 0.005	7.8 ± 1.7	-6.4 ± 1.7	P
GOODS-N	25142	2.4691	0.240 ± 0.011	-40.6 ± 6.0	-9.2 ± 2.6	С

Table 1 (Continued)

Field	ID	Redshift	E(B-V)	$\mathrm{EW}_{\mathrm{Ly}lpha} \ (\mathrm{\mathring{A}})$	EW _{LIS} (Å)	LIS Category
GOODS-N	25688	2.3748	0.070 ± 0.005	0.6 ± 0.4	-7.5 ± 0.5	D
GOODS-N	26621	2.3055	0.090 ± 0.005	-31.0 ± 3.8	-7.0 ± 1.5	P
GOODS-N	27035	2.4218	0.080 ± 0.005	-22.1 ± 4.5	-7.6 ± 2.1	P
GOODS-N	28237	2.2266	0.080 ± 0.008	-3.1 ± 0.8	>-2.3	L
GOODS-N	28599	1.6871	0.090 ± 0.005	3.6 ± 4.6	-6.4 ± 2.1	C
GOODS-N	28846	2.4720	0.090 ± 0.006	3.1 ± 1.8	-5.5 ± 1.9	P
GOODS-N	29743	2.1867	0.210 ± 0.009	13.0 ± 2.2	-8.4 ± 1.0	D
GOODS-N	30053	2.2452	0.320 ± 0.011	6.5 ± 5.0	-12.8 ± 3.6	P
GOODS-N	32526	2.4088	0.100 ± 0.010	-23.7 ± 15.3	>-10.8	L
GOODS-S	31344	2.3237	0.230 ± 0.007	-6.0 ± 1.2	-9.8 ± 1.0	D
GOODS-S	31854	2.4250	0.080 ± 0.005	-5.0 ± 1.2	-4.2 ± 1.3	C
GOODS-S	32837	2.0608	0.065 ± 0.006	-4.0 ± 0.9	-5.7 ± 1.2	P
GOODS-S	33248	2.3245	0.090 ± 0.008	-23.8 ± 5.8	>-4.3	L
GOODS-S	35178	2.4084	0.100 ± 0.005	-11.3 ± 3.3	-7.8 ± 2.6	P
GOODS-S	35705	2.3234	0.150 ± 0.008	-0.5 ± 1.2	-6.3 ± 1.6	P
GOODS-S	35779	2.2536	0.050 ± 0.005	5.2 ± 1.4	-7.1 ± 2.4	P
GOODS-S	36705	2.3064	0.130 ± 0.006	3.5 ± 0.4	-7.6 ± 0.4	D
GOODS-S	37988	2.2008	0.330 ± 0.009	-14.6 ± 1.6	>-6.6	L
GOODS-S	38116	2.1968	0.260 ± 0.009	-21.7 ± 4.9	-7.8 ± 1.9	P
GOODS-S	38559	2.1939	0.080 ± 0.005	2.8 ± 0.9	-5.5 ± 0.9	D
GOODS-S	39198	2.5789	0.030 ± 0.005	12.3 ± 0.5	-5.3 ± 1.3	P
GOODS-S	39713	2.1546	0.050 ± 0.006	10.2 ± 1.1	-7.4 ± 0.9	D
GOODS-S	40218	2.4508	0.080 ± 0.005	-8.0 ± 0.6	-7.9 ± 0.4	D
GOODS-S	40679	2.4087	0.280 ± 0.009	-10.9 ± 3.6	-9.1 ± 2.8	P
GOODS-S	40768	2.3035	0.190 ± 0.010	-36.0 ± 1.5	-14.4 ± 0.7	D
GOODS-S	41547	2.5451	0.060 ± 0.005	-12.4 ± 0.5	-7.5 ± 0.3	D
GOODS-S	42363	2.1411	0.210 ± 0.009	-6.2 ± 1.1	-14.2 ± 0.8	D
GOODS-S	42809	2.2494	0.020 ± 0.005	12.9 ± 1.0	-3.6 ± 0.9	P
GOODS-S	45180	2.2858	0.090 ± 0.005	7.7 ± 2.2	-8.8 ± 3.1	P
GOODS-S	45531	2.3116	0.040 ± 0.005	13.2 ± 0.5	-5.4 ± 0.5	D
GOODS-S	46938	2.3325	0.060 ± 0.003	22.6 ± 0.9	-6.5 ± 0.2	D

Note. The EW values listed are in the rest frame. The LIS EW represents the sum of Si II λ 1260, O I λ 1302+Si II λ 1304, and C II λ 1334. For LIS nondetections, a 3σ limit is reported. The LIS category denotes how the LIS EW was calculated: "D" represents the cases where all three lines are individually detected, "P" represents where only one or two LIS lines are detected at the \geq 3 σ level and the LIS EW was inferred based on the method described in Section 3.2.2, "C" represents where none of the LIS lines were individually detected but the combined line S/N is \geq 3, and "L" represents where none of the LIS lines were individually detected and the combined line S/N is <3, therefore a limit is reported.

(This table is available in machine-readable form.)

density level. Although by construction, all galaxies in the LRIS-ISM sample have $\mathrm{Ly}\alpha$ coverage, four galaxies (one "emission" and three "noise" objects) have no spectral coverage at rest-frame wavelengths shorter than 1160 Å, such that the spectral region available is not sufficient (less than 20 Å) for a robust estimate of the blue-side continuum level. Consequently, in each $\mathrm{Ly}\alpha$ morphology category, we measured the relative level of the blue-and red-side continua from objects with adequate spectral coverage on both sides. The median blue-to-red continuum ratio in the corresponding $\mathrm{Ly}\alpha$ morphology category was then applied as a rough proxy of the blue continuum for those four objects lacking sufficient blue-side spectral coverage.

To characterize the uncertainty on the Ly α EW, we perturbed the science spectrum 100 times with its corresponding error spectrum and measured the Ly α EW in the 100 fake spectra for each galaxy. The σ -clipped average and standard deviation of those 100 measurements were adopted as the final Ly α EW and 1 σ uncertainty, respectively, for each galaxy. We list the measured rest-frame Ly α EW for all 157 galaxies in the LRIS-ISM sample in Table 1.

3.2.2. LIS Lines

Our deep LRIS spectra enable LIS line measurements from individual objects in the LRIS-ISM sample. In this study, we focus on the EW of the three LIS lines near Ly α : Si II λ 1260, O I λ 1302+Si II λ 1304, and C II λ 1334. These lines are among the strongest rest-UV LIS features and typically saturated in the MOSDEF-LRIS sample. Provided that we require measurements of EW_{LV\alpha} and EW_{LIS}, measuring these three lines would maximize the sample size because of their proximity to the Ly α feature. Given the low resolution of the blue-side LRIS spectra, O I λ 1302+Si II λ 1304 is blended in the individual spectra. As in Du et al. (2016), we adopted single-component Gaussian fits as the simplest but sufficient functional form to describe the interstellar absorption line profiles because the data are not of sufficient resolution to consider more complex models. We have further tested that for obtaining EW measurements, single-component Gaussian fits yield almost identical results to those suggested by two-component fits (i.e., two independent Gaussians describing the systemic and outflowing components, respectively).

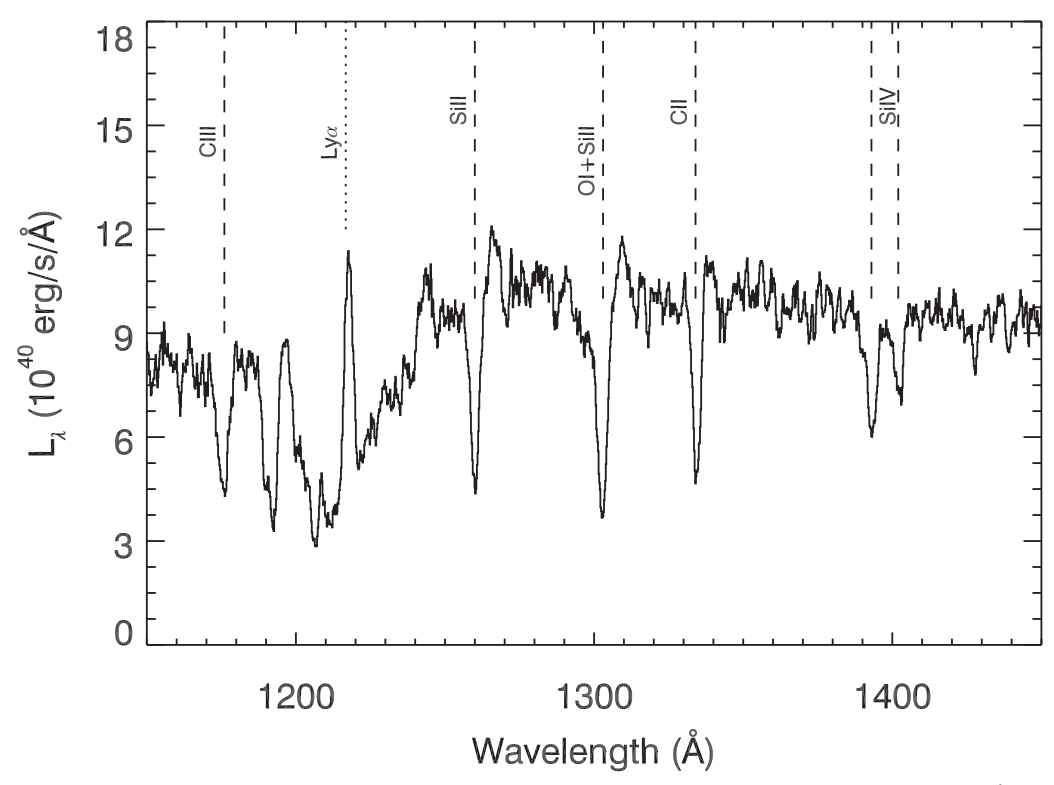


Figure 1. Composite rest-frame far-UV spectrum of the 157 galaxies in the LRIS-ISM sample. We show the rest-frame 1150-1450 Å portion of the composite spectrum, as only the spectral region from Ly α to C II $\lambda 1334$ has a contribution from all 157 galaxies. Key emission (dotted lines) and absorption (dashed lines) features in this range are labeled.

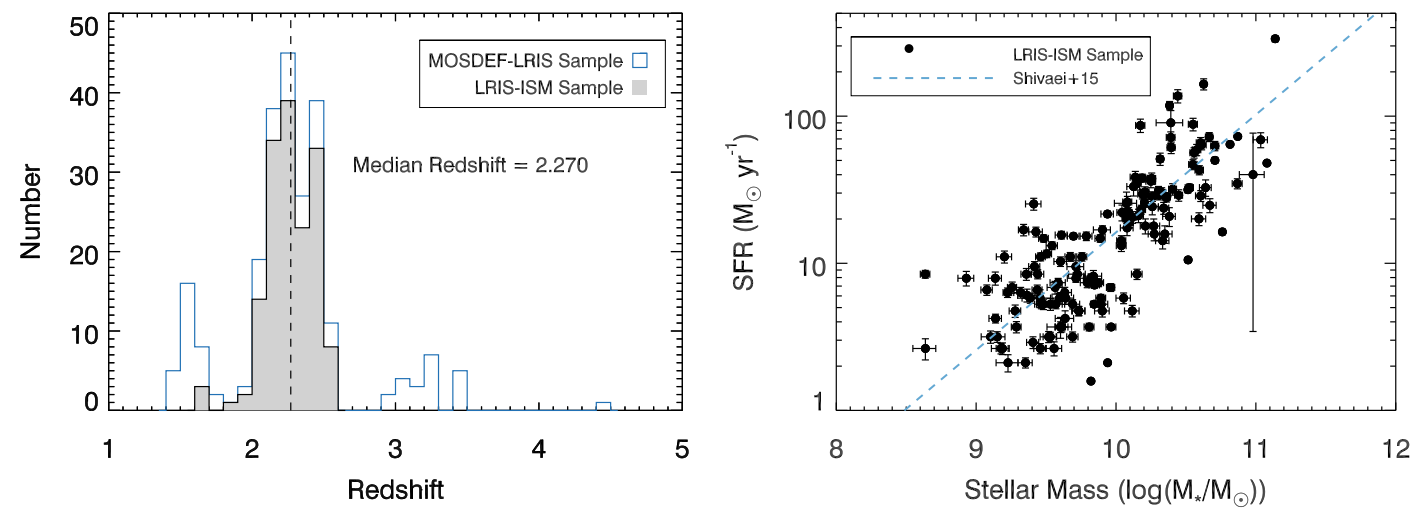


Figure 2. Galaxy properties of the LRIS-ISM sample. Left: redshift distribution. Open blue and filled gray bars represent the parent MOSDEF-LRIS sample with redshift measurements (from either MOSFIRE or LRIS; 236 objects) and the LRIS-ISM sample (157 objects), respectively. The vertical dashed line marks the median redshift of the LRIS-ISM sample. Right: SFR vs. stellar mass. Both SFR and stellar mass are derived from SED modeling assuming a Chabrier IMF, as described in Section 3.1. Error bars in SFR and stellar mass indicate the associated 1σ uncertainties. For comparison, we indicate with a blue dashed line the SFR vs. stellar mass relation derived in Shivaei et al. (2015) using objects with $M_* > 10^{9.5} M_{\odot}$ in the parent MOSDEF sample. While Shivaei et al. (2015) presented multiple SFR estimates (e.g., UV-, Hα-, and SED-based), we only plot those based on SED modeling for a direct comparison with our work.

We continuum-normalized the rest-frame spectra using spectral windows that are clean of spectral features defined by Rix et al. (2004). Based on these windows, we modeled the continuum for all individual spectra with the IRAF *continuum* routine using a *spline 3* function of order = 8. Regions near Ly α (1197–1248 Å) were not used for estimating the continuum, as the continuum is fairly curved near that region and affected by the broad Ly α absorption trough for the

"absorption" and "combination" objects. In cases where the fitted continuum level did not provide a proper description of the observed spectrum due to the limited coverage of windows from Rix et al. (2004), additional windows customized for each object were added to provide reasonable constraints on the fit.

The absorption line profile fitting was performed on the continuum-normalized individual spectra. For the "detection", "partial detection", and "combined detection" objects (see

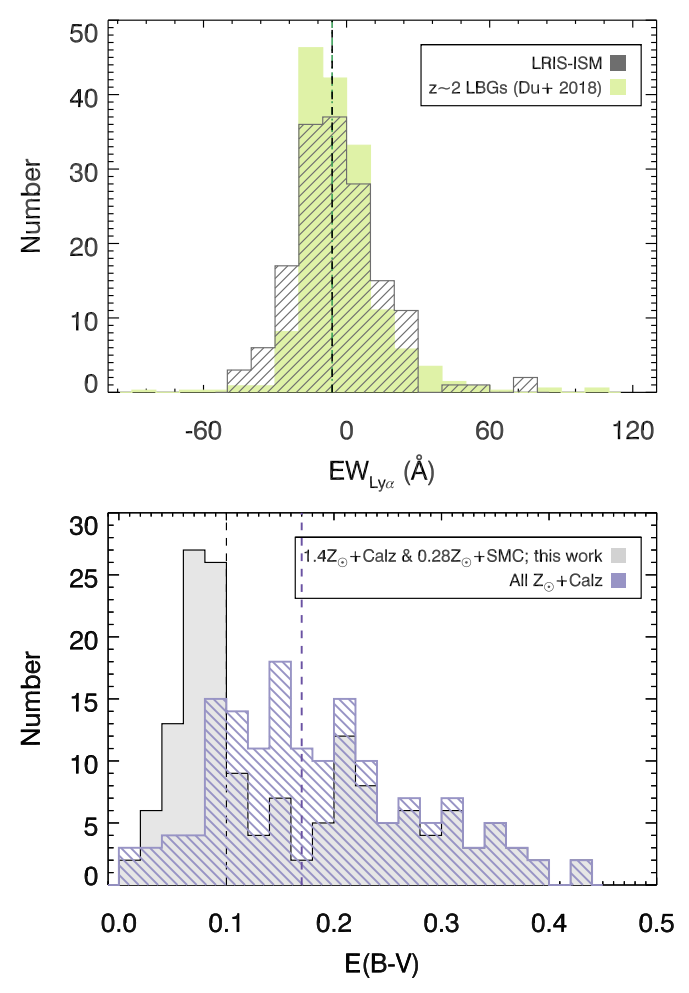


Figure 3. Top: rest-frame Ly α EW distribution. The filled green bar indicates the $z\sim2$ LBG sample (538 objects) presented in Du et al. (2018), normalized to the same total number as the LRIS-ISM sample (157 objects; hatched gray bar). The median EWs are -6.0 and -6.1 Å for the LRIS-ISM and $z\sim2$ LBG samples, respectively, shown with a dashed black line for the former and a dashed—dotted green line for the latter. Bottom: E(B-V) distribution. The filled gray bar shows the distribution of E(B-V) estimated based on the 1.4 Z_{\odot} +Calzetti (0.28 Z_{\odot} +SMC) model for objects above (below) stellar mass log $(M_*/M_{\odot})=10.04$, following the stellar population modeling procedures described in Section 3.1. The median E(B-V) is 0.10, as denoted by the vertical dashed black line. In comparison, the E(B-V) distribution derived by fitting all objects with the 1.4 Z_{\odot} +Calzetti model is plotted with the hatched purple bar. The corresponding median E(B-V) is 0.17 (purple dashed line).

descriptions below), we used the IDL program MPFIT (Markwardt 2009) with the initial values of the continuum flux level, line centroid, EW, and Gaussian FWHM estimated from the program splot in IRAF. The best fit was then determined, where the χ^2 of the fit reached a minimum. We iterated the fitting over a narrower wavelength range for all of the interstellar absorption lines: centroid $-4\sigma < \lambda <$ centroid $+4\sigma,$ where the centroid and σ are, respectively, the returned central wavelength and standard deviation of the best-fit Gaussian profile from the initial MPFIT fit to respective lines over $\lambda_{\rm rest}-10~{\rm \AA}$ to $\lambda_{\rm rest}+10~{\rm \AA}.$

Ideally, we would like to measure Si II, O I+Si II, and C II individually and take the sum of their EWs as the EW_{LIS} for each object. However, not all three lines are detected at the $\geqslant\!3\sigma$ level for every galaxy in the LRIS-ISM sample. Therefore, we inferred the total LIS EW differently for objects in four different LIS categories.

Detection. Fifty-one out of 157 objects, marked as "D" in Table 1 and the figures in Section 4. In the spectra for these objects, all three LIS lines are individually detected. Therefore, the total EW of the LIS lines was adopted as EW_{LIS} for such objects, and the 1σ uncertainty was estimated by adding the 1σ error bar of all three LIS lines in quadrature.

Partial detection. Sixty-one out of 157 objects, marked as "P." In the spectra for these objects, one or two LIS lines are individually detected, even though we required all three LIS lines to be covered in individual galaxy spectra. This is because we excluded particular LIS lines in a small number of cases when they were clearly contaminated or showed an unphysical absorption profile (e.g., significantly negative at maximum depth). Given that the LIS lines are typically saturated in star-forming galaxies with properties typical of those in our sample (e.g., Shapley et al. 2003), their EWs are not sensitive to column density but rather the combination of the covering fraction and velocity dispersion of the respective ions. To that end, we expect that the lines we measure here (Si II, O I+Si II, and C II) have the same relative strengths across this category, assuming all low ions have similar covering fractions and velocity dispersions. For "partially detected" objects, the undetected LIS lines primarily result from systematic errors or artifacts in the spectra but not their weaker nature. To infer the total EW_{LIS}, we calculated f_i , the fractional contribution of the EW of absorption line i to EW_{LIS} in the sample of "detection" objects. Explicitly, $f_i = EW_i/EW_{LIS}$, where i denotes the respective LIS lines and EW_i is the measured EW of that line. The median f values and associated uncertainties, Δf , for Si II, O I+Si II, and C II are, respectively, 0.285 ± 0.063 , 0.422 ± 0.077 , and 0.287 ± 0.056 , where the uncertainties were estimated from error propagation. Those median f values were used to scale the measured partial EWs to a "total" EW_{LIS}. For example, in the case of an object with only a detected O I λ 1302 +Si II λ 1304 line, we calculated EW_{LIS} by dividing the O I+Si II EW by 0.422. Similarly, for an object with detections in Si II $\lambda 1260$ and C II $\lambda 1334$, we calculated its EW_{LIS} by dividing the sum of the Si II and C II EWs by 0.285 + 0.287 = 0.572. The uncertainty on the inferred total EW_{LIS} for individual objects was obtained through propagation of error using the following equation, determined from the sample of "detected" objects:

$$\Delta EW_{LIS} = EW_{LIS} \sqrt{\left(\frac{\Delta f_i}{f_i}\right)^2 + \left(\frac{\Delta EW_i}{EW_i}\right)^2},$$
 (1)

where ΔEW_i represents the measurement uncertainty of line i (when only one line is detected) or the combination of lines (e.g., Si II λ 1260 and C II λ 1334; when two lines are detected). The fractional contributions of a combination of two detected lines to EW_{LIS} are 0.713 ± 0.111 , 0.715 ± 0.110 , and 0.578 ± 0.094 for Si II λ 1260+O I λ 1302+Si II λ 1304, O I λ 1302+Si II λ 1304+C II λ 1334, and Si II λ 1260+C II λ 1334, respectively.

The above method of determining the overall uncertainty on $\mathrm{EW}_{\mathrm{LIS}}$ based on partial information accounts for not only the measurement uncertainties from individual LIS lines but also that associated with the respective scaling factors, f. As described below, we adopted the same error estimate method for the "combined detection" and "limit" objects when not all three LIS lines are available. We note that the absolute values of the LIS measurement uncertainties do not affect the relative strengths of the mutual correlations among $\mathrm{EW}_{\mathrm{Ly}\alpha}$, $\mathrm{EW}_{\mathrm{LIS}}$, and

E(B-V), as suggested by additional ASURV tests (see Section 4.3 for details).

Combined detection. Twelve out of 157 objects, marked as "C." While no LIS lines are individually detected, the combined line S/N (from two or three lines) is \geqslant 3. For objects with all three lines available, the total EW and the associated 1σ uncertainty on EW_{LIS} were estimated using the same method as for the "detection" objects. In cases where only two lines were available and showed a combined line S/N \geqslant 3, we computed its total EW and the associated 1σ uncertainty by scaling them using the same corresponding factors calculated in the "partial detection" category (see above).

Limit. Thirty-three out of 157 objects, marked as "L." In this category, objects have no LIS lines individually detected, and the combined line S/N (from one, two, or three lines) is <3. Considering that the nondetected LIS lines may not have a well-defined Gaussian profile, we performed simple integration over a spectral range of ± 2 Å from the rest-frame wavelength of each LIS line on the continuum-normalized spectra. This 4 Å wide window has been tested to be sufficient to capture the LIS nondetections based on the typical width of LIS features measured at the 2σ - 3σ level in individual continuum-normalized spectra. For objects in the "limit" category, we report a 3σ upper limit in EW_{LIS}. We note that, in such cases, EW_{LIS} is plotted in figures as a lower limit, since we define LIS absorption as negative. The 1σ uncertainty on EW_{LIS} was estimated by adding the 1σ error bar of all available LIS lines in quadrature, where the error bar on an individual LIS EW was calculated by adding the continuum-normalized flux density level at each wavelength in quadrature in the corresponding error spectrum over the same spectral region used for the flux integration (i.e., line centroid $\pm 2\,\text{Å}$). In cases where only one or two LIS lines are available, we scaled the limit using the same corresponding factors calculated in the "partial detection" category (see above).

In summary, 71% of the LRIS-ISM sample has EW_{LIS} inferred from robust detections of one or more lines, while only 21% has limits and 8% requires combining LIS lines to yield a detection. Obtaining robust LIS measurements from firm detections for a large majority of the sample enables us to examine the intrinsic scatter of the relations presented in Section 4 from an individual-object perspective.

4. Results

4.1. Ly α and E(B - V) Distributions

Rest-frame EW_{Ly\alpha} and E(B-V) were measured using the methods described in Section 3 for all objects in the LRIS-ISM sample. The individual Ly\alpha measurements are listed in Table 1. As shown in the top panel of Figure 3, the Ly\alpha EW ranges from -47.3 to 78.0 Å with a median of -6.0 Å. The median EW_{Ly\alpha} of the *H*-band-selected LRIS-ISM sample is similar to that of the $z\sim2$ UV-selected LBG sample presented in Du et al. (2018), and the EW_{Ly\alpha} distribution of the LRIS-ISM sample is slightly wider (the standard deviations are 19.1 and 18.0 Å, respectively, for the LRIS-ISM and $z\sim2$ LBG EW_{Ly\alpha} distributions).

As for dust attenuation, the derived E(B-V) value for the LRIS-ISM sample ranges from 0.01 to 0.435 with a median of 0.10. This median E(B-V) value is very close to that of the $z \sim 2$ LBG sample (median E(B-V) = 0.09) in Du et al. (2018), in which similar SED modeling approaches were

adopted. We note that the 1.4 Z_{\odot} +Calzetti model outputs a systematically higher E(B-V) than the 0.28 Z_{\odot} +SMC model for the same galaxy SED; hence, the peak shown near $E(B-V) \sim 0.08-0.10$ in Figure 3 is caused by the adoption of the 0.28 Z_{\odot} +SMC model (smaller E(B-V)) for lower-mass galaxies. Assuming the 1.4 Z_{\odot} +Calzetti model for all objects in the sample would result in a flatter distribution with a median E(B-V) = 0.17. However, as justified in Section 3.1, we believe that the 0.28 Z_{\odot} +SMC model better characterizes the lower-mass (log (M_*/M_{\odot}) < 10.04) galaxies in our sample. Additionally, as the E(B-V) values derived from the 1.4 Z_{\odot} +Calzetti and 0.28 Z_{\odot} +SMC models are tightly correlated, adopting a combination of these two models would not considerably change the dust extinction among the galaxies in a relative sense (i.e., galaxies with a higher-than-average E(B-V) output by the 1.4 Z_{\odot} +Calzetti model still have a relatively high E(B-V) derived from the 0.28 $Z_{\odot}+SMC$ model). As a result, the qualitative trends between E(B-V)and both $EW_{Ly\alpha}$ and EW_{LIS} (Section 4.2) should not be significantly affected.

4.2. Relations among EW_{Lyco} , EW_{LIS} , and E(B-V)

One key aspect of this study is to quantify the relative tightness of the relations among $EW_{Ly\alpha}$, EW_{LIS} , and E(B-V) using measurements from individual galaxies. To avoid potential bias introduced by selection effects, we conducted statistical analysis using the entire LRIS-ISM sample (157 objects), which includes 33 limits in EW_{LIS}. With the measurements of EW_{Ly α}, EW_{LIS}, and E(B-V) obtained in Section 3, we plot the relations among these three parameters in Figure 4. To parameterize the correlations, we used the IDL package LINMIX_ERR (Kelly 2007) for performing a linear regression between each pair of observables. The linear function takes the form $y = intercept + slope * x + \epsilon$, where ϵ represents the intrinsic random scatter in the regression and is a normal distribution with a zero mean. LINMIX_ERR is an ideal program for dealing with complex data like ours, as it not only takes into account the measurement uncertainties in both variables but also allows censored data (i.e., nondetections). The program adopts a Bayesian approach for calculating the linear regression, and each parameter (such as intercept, slope, and intrinsic scatter) is returned as an array of 200 draws from its associated posterior distribution. We report the regression coefficients in Table 2, where the reported values and error bars were determined based on the median and standard deviation of the 200 draws of the respective parameter.

The regression coefficients in Table 2 suggest that $\mathrm{EW}_{\mathrm{Ly}\alpha}$ is larger in galaxies with smaller $\mathrm{EW}_{\mathrm{LIS}}$ and E(B-V), and $\mathrm{EW}_{\mathrm{LIS}}$ increases with increasing E(B-V). These qualitative findings are consistent with previous work at similar redshifts using galaxy composite spectra (e.g., Shapley et al. 2003; Du et al. 2018). However, our results represent the first such analysis of the mutual correlations among $\mathrm{EW}_{\mathrm{Ly}\alpha}$, $\mathrm{EW}_{\mathrm{LIS}}$, and E(B-V) based on individual measurements at high redshift, enabling an investigation of the scatter in these key relationships.

While the "intrinsic scatter" term can be useful in quantifying the tightness of the correlations, the values returned by LINMIX_ERR describe the deviation in the y-axis and can only be used for direct comparison if the dependent variable is the same. Given that $\mathrm{EW}_{\mathrm{Ly}\alpha}$ and $\mathrm{EW}_{\mathrm{LIS}}$ can be the dependent variable in different correlations, and that their dynamic ranges and distributions are drastically different, we therefore seek

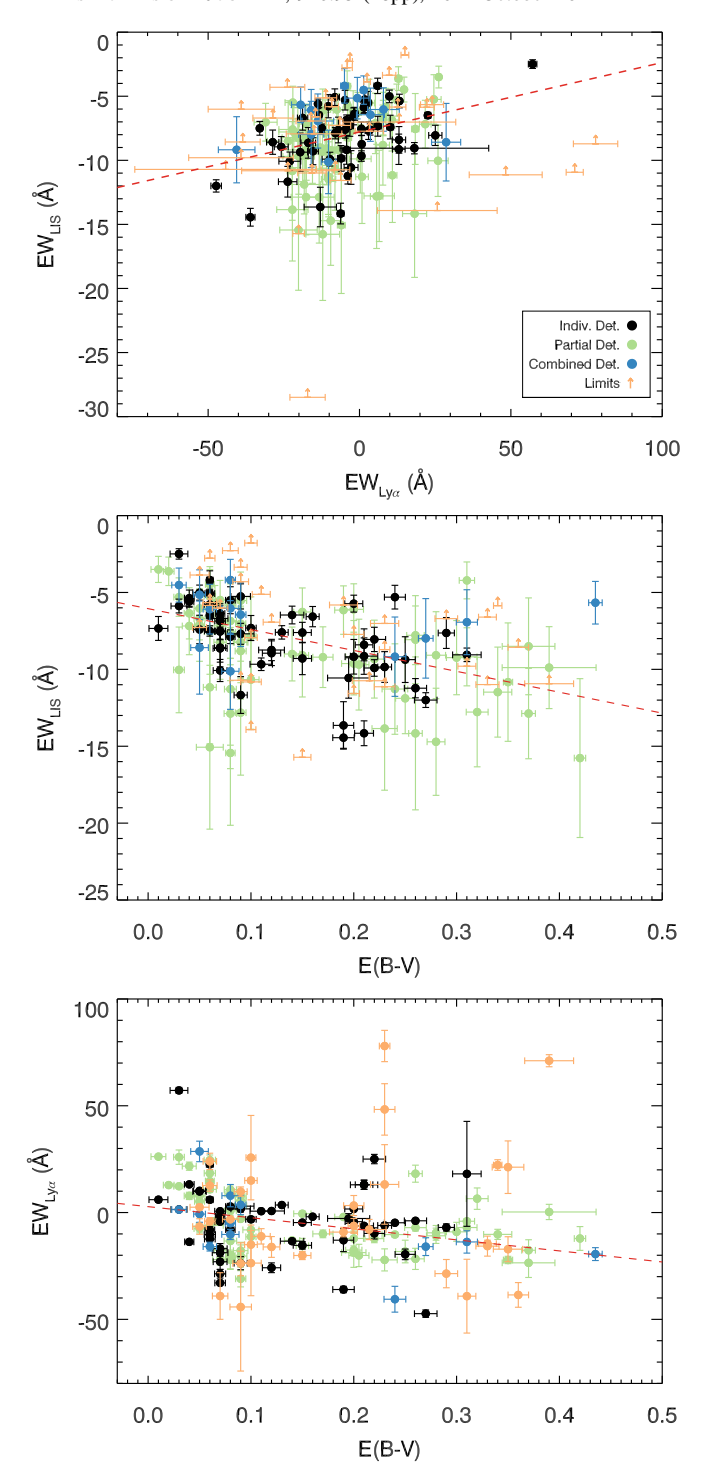


Figure 4. Correlations among $EW_{Ly\alpha}$, EW_{LIS} , and E(B-V) using individual measurements from 157 galaxies in the LRIS-ISM sample. Top: EW_{LIS} vs. $EW_{Ly\alpha}$. The black, green, and blue circles show the objects with individual (51 objects), partial (61 objects), and combined (12 objects) detections, as classified in Section 3.2.2. The 1σ error bar is plotted for the detections. The orange upward-pointing arrows denote the 3σ limit on EW_{LIS} for 33 objects where the LIS lines are not significantly detected. The limits are plotted as lower limits, as we define absorption line EW as negative. The dashed red line marks the best-fit linear regression, returned by LINMIX_ERR (see Section 4.2). Middle: EW_{LIS} vs. E(B-V). The color coding of the symbols is the same as in the top panel. Bottom: $EW_{Ly\alpha}$ vs. E(B-V). The color coding of the symbols is the same as in the top panel, except that the EW_{LIS} limits are plotted as circles, as those 33 objects all have measured $EW_{Ly\alpha}$ and E(B-V).

Table 2
Linear Regression Coefficients

Correlation	Intercept (Å)	Slope	Intrinsic Scatter ^a (Å)
	Entire Samp	le (157 Objects)	
$EW_{LIS} \text{ vs.}$ $E(B-V)$	-6.086 ± 0.397	-12.871 ± 2.511	1.816 ± 0.191
${ m EW}_{ m LIS}$ vs. ${ m EW}_{ m Lylpha}$	-7.759 ± 0.198	0.062 ± 0.012	1.916 ± 0.170
$\frac{EW_{Ly\alpha} \text{ vs.}}{E(B-V)}$	3.037 ± 2.353	-53.813 ± 12.682	14.649 ± 0.913

Note

alternative programs for performing statistical analysis on the correlations (see Section 4.3).

4.3. Relative Strengths of the Key ISM/CGM Relations

To utilize the entire sample and directly compare the relative tightness of the mutual correlations among EW_{Lv\alpha}, EW_{LIS} , and E(B-V), we adopted the FORTRAN routine ASURV (Feigelson & Nelson 1985; Isobe et al. 1986; Isobe & Feigelson 1990; Lavalley et al. 1992) for performing survival analysis of censored data, which was written specifically to treat nondetections due to sensitivity limits. ASURV offers various statistical tests, out of which we chose to use the generalized Kendall's τ and Spearman's ρ correlation coefficients for characterizing the tightness of the correlations. Both correlation coefficients assess statistical associations based on the ranks of the data and yield almost identical results for our sample. The resulting Kendall's τ and Spearman's ρ are listed in Table 3, along with the corresponding probability of a null hypothesis (i.e., that the data are uncorrelated).

One complication in using ASURV is that the routine does not consider measurement uncertainties on the variables, but all of our measurements have associated 1σ error bars except for the EW_{LIS} nondetections (in which case, a 3σ limit was fed to ASURV). To account for the measurement uncertainties, for each correlation (EW_{LIS} versus EW_{Ly\alpha}, EW_{Ly\alpha} versus E(B-V)), or EW_{LIS} versus E(B-V)), we perturbed the detections in both variables by their individual error bars 100 times while keeping the 3σ limit of the nondetections unchanged. The standard deviation of those 100 realizations on Kendall's τ , Spearman's ρ , and the P_K and P_{SR} values was taken as the error bar on the respective parameters in Table 3 to reflect the uncertainty on the statistical analysis results introduced by measurement errors.

The statistical tests show that $\mathrm{EW}_{\mathrm{Ly}\alpha}$, $\mathrm{EW}_{\mathrm{LIS}}$, and E(B-V) are intercorrelated. All three correlations have a $>3\sigma$ significance, but the $\mathrm{EW}_{\mathrm{LIS}}$ versus E(B-V) relation is the strongest. The strengths between $\mathrm{EW}_{\mathrm{Ly}\alpha}$ versus $\mathrm{EW}_{\mathrm{LIS}}$ and $\mathrm{EW}_{\mathrm{Ly}\alpha}$ versus E(B-V) are comparable considering the uncertainty on the correlation coefficients, with the former being slightly weaker. We note that swapping the x- and y-axis observables (e.g., from $\mathrm{EW}_{\mathrm{LIS}}$ versus

^a The linear regression assumes the form $y = \text{intercept} + \text{slope} * x + \epsilon$, where ϵ follows a normal distribution with zero mean and variance equal to the square of the intrinsic scatter.

Table 3Correlation Coefficients

Correlation	Kendall τ^a	P_K^{b}	Spearman ρ^{a}	$P_{\rm SR}^{}$
		Entire Sample (157 Objects)		
EW_{LIS} vs. $E(B-V)$	5.301 ± 0.557	0.0000 ± 0.0000^{c}	-0.396 ± 0.042	0.0000 ± 0.0007
$\overline{\text{EW}_{\text{LIS}}}$ vs. $\overline{\text{EW}_{\text{Ly}lpha}}$	3.520 ± 0.503	0.0004 ± 0.0066	0.273 ± 0.038	0.0006 ± 0.0090
$EW_{Ly\alpha}$ vs. $E(B-V)$	3.859 ± 0.248	0.0001 ± 0.0001	-0.299 ± 0.019	0.0002 ± 0.0002
		Only LIS Detections (124 Objects) ^d		
EW_{LIS} vs. $E(B-V)$	6.340 ± 0.655	0.0000 ± 0.0000	-0.531 ± 0.053	0.0000 ± 0.0000
$\overline{\text{EW}_{\text{LIS}}}$ vs. $\overline{\text{EW}_{\text{Ly}lpha}}$	3.862 ± 0.581	0.0001 ± 0.0074	0.345 ± 0.051	0.0001 ± 0.0082
$\overline{\mathrm{EW}_{\mathrm{Ly}\alpha}} \text{ vs. } E(B-V)$	4.505 ± 0.272	0.0000 ± 0.0000	-0.391 ± 0.023	0.0000 ± 0.0000

Notes.

^d The EW_{LIS} detections include the "D," "P," and "C" objects, as defined in Section 3.2.2.

E(B-V) to E(B-V) versus EW_{LIS}) yields similar correlation coefficients and does not change the relative strength of the mutual correlations we examine here. Provided that the $EW_{Ly\alpha}$ versus E(B-V) relation does not contain any measurement limits but the other two relations do, we also tested whether excluding the limits would change the results. We performed similar statistical analyses using ASURV on the 124 objects with detected LIS features (including the individual, partial, and combined detections as described in Section 3.2.2). When considering detections only, the correlation between EW_{LIS} and E(B-V) is again the strongest, while that between $EW_{Ly\alpha}$ and EW_{LIS} is the weakest. Therefore, including limits does not change the relative tightness of the three correlations.

Our results suggest that the most direct connection exists between the HI covering fraction and dust attenuation, as probed by EW_{LIS} and E(B-V), respectively. The EW_{Ly α} versus E(B-V) correlation is the second strongest, highlighting the preferential dust extinction of Ly α photons relative to continuum photons within the region covered by the LRIS spectroscopic slit. Alternatively, the observed $EW_{Ly\alpha}$ versus E(B-V) trend can be explained by more scattering of Ly α photons out of the spectroscopic slit by the higher H I covering fraction typically associated with higher E(B-V). Finally, although the weakest among the three, the correlation between EW_{LIS} and $EW_{Ly\alpha}$ points to the impact of resonant scattering on the emergent Ly α emission when Ly α photons travel through HI clouds. The relatively large scatter in the EW_{LIS} versus $EW_{Lv\alpha}$ relation compared to the other two suggests the galaxy-to-galaxy variation when using LIS lines as a probe to trace HI, as we investigate in Section 5.2.1. We discuss in detail the astrophysical picture suggested by our results in Section 5.1.

5. Discussion

We have shown in Section 4 that $\mathrm{EW}_{\mathrm{Ly}\alpha}$, $\mathrm{EW}_{\mathrm{LIS}}$, and E(B-V) are intercorrelated. While all three relations are statistically significant, the tightest correlation is found between $\mathrm{EW}_{\mathrm{LIS}}$ and E(B-V). This particular result highlights the direct connection between dust and metal-enriched H I gas, suggesting that they are likely to be cospatial. Additionally, the $\mathrm{EW}_{\mathrm{Ly}\alpha}$

versus EW_{LIS} correlation is found to be weaker than that between EW_{LIS} and E(B-V). This finding differs from the speculation made by multiple previous studies that $EW_{Ly\alpha}$ and EW_{LIS} are the most directly connected (Shapley et al. 2003; Du et al. 2018). Although the strength of $Ly\alpha$ is directly modulated by the covering fraction of H I gas through resonant scattering, noticeable scatter can be introduced to the $EW_{Ly\alpha}$ versus EW_{LIS} relation by the object-to-object variation in the metal-to-H I covering fraction ratio (see a detailed discussion in Section 5.2.1). Lastly, as detailed in Sections 5.1.2 and 5.2.2, we identify the dust content between the H I gas clumps and outflow kinematics as two key contributors to the scatter in the $EW_{Ly\alpha}$ versus E(B-V) relation.

In this section, we review two ISM/CGM models involving the physical distributions of neutral hydrogen gas, dust, and metals. The empirical results presented in Section 4 can be interpreted with reference to these ISM/CGM models, leading to insights into the distribution and kinematics of interstellar and circumgalactic gas, metals, and dust and the escape of ionizing and $\text{Ly}\alpha$ photons. We then discuss the origins of the intrinsic scatter in the correlations observed among $\text{EW}_{\text{Ly}\alpha}$, EW_{LIS} , and E(B-V).

5.1. ISM/CGM Models

The physical picture underlying the observed trends among EW_{LVO} , EW_{LIS} , and E(B-V) at $z \sim 2-4$ has been considered in previous work (e.g., Shapley et al. 2003; Jones et al. 2012; Du et al. 2018). In such descriptions, LIS absorption arises from metal-enriched clouds, which exist within a medium of patchy, neutral hydrogen gas. The ISM/CGM is considered porous due to the presence of outflows induced by active star formation commonly observed at high redshift (Pettini et al. 2001; Shapley et al. 2003; Steidel et al. 2004). While Ly α photons are resonantly scattered by the H I gas, they eventually escape through "holes" in the HI gas where the HI column density or covering fraction is low or by being backscattered off of receding gas on the far side of the outflow. At the same time, we must consider the dust content of the absorbing HI gas in this picture, which is responsible for attenuating both the UV continuum and Ly α photons.

^a Test statistic. The uncertainties on the correlation coefficients and P-values were derived by perturbing the measurements by their associated error bars.

^b Probability of a null hypothesis.

 $^{^{\}rm c}$ A P_K or $P_{\rm SR}$ value or uncertainty listed as 0.0000 indicates an actual value less than 10^{-4} (but nonzero) and below the limit of precision offered by ASURV.

We do not yet have a clear picture, however, of the structure of the CGM and where dust resides with respect to the H I gas in the ISM/CGM of typical star-forming galaxies at high redshift. As dust grains are formed by the condensation of metals, the distributions of metals and dust are expected to be highly correlated spatially. Two basic CGM models that have been examined by previous studies (e.g., Vasei et al. 2016; Gazagnes et al. 2018; Steidel et al. 2018) include (1) a picketfence H I gas model with a uniform foreground dust screen and (2) a clumpy H I gas model where dust and metals are only located in the HI gas clumps. We note that in both models described above, the neutral hydrogen gas is always considered "picket fence-like" with a nonunity covering fraction, and the major difference lies in the distribution of dust and metals in the ISM/CGM. In this section, we compare our results with the model predictions and discuss which model our results are most likely to support.

5.1.1. Uniform Dust Screen Model

As described in previous work (Vasei et al. 2016; Gazagnes et al. 2018; Steidel et al. 2018), the uniform dust screen model assumes that patchy H I gas in the ISM is dust- and metal-free, whereas dust, along with the metals that give rise to the low ions, exists in a foreground, uniform screen. If dust is uniformly distributed in and only in the foreground with a 100% covering fraction, the attenuation affects both Ly α photons and the UV continuum to the same extent. The observed Ly α flux originates from the escaped Ly α photons, either directly from the Ly α -emitting region or after multiple resonant scattering events, through channels of HI gas with a low covering fraction or column density. In this work, we used $EW_{Lv\alpha}$ (instead of $Ly\alpha$ flux) as an observable, which is defined as the ratio of integrated Ly α flux and the continuum flux density redward of Ly α . As the uniform dust screen attenuates the observed Ly α flux and the continuum to the same degree, the resulting EW_{Ly α} should be uncorrelated with E(B-V) and only dependent on the HI covering fraction. Our results, however, contradict this prediction. We observe a significant anticorrelation between $EW_{Ly\alpha}$ and E(B-V), where $EW_{Ly\alpha}$ decreases with increasing E(B-V), which would not occur if dust only existed in a uniform foreground screen but not in the HI gas clumps.

In addition, the assumptions in the dust screen model suggest that the covering fractions of dust and H I gas are independent; the H I covering fraction can vary, while the dust covering fraction is always 100%. Studies have shown that the metal covering fraction is positively correlated with the H I covering fraction (Reddy et al. 2016; Gazagnes et al. 2018), providing justification for using metal lines to probe HI gas. If the covering fractions of dust and HI gas were truly independent, EW_{LIS} and E(B-V) would display no apparent correlation. On the contrary, our findings show not only that EW_{LIS} and E(B-V) are correlated but that their correlation is the strongest among the three key relations highlighted in this work (i.e., those connecting $EW_{Ly\alpha}$, EW_{LIS} , and E(B-V)). This strong connection between $\acute{E}W_{LIS}$ and E(B-V) points to the possibility that the metal-enriched H I gas and dust may in fact be cospatial. Finally, we caution that the uniform dust screen model is not very probable in an astrophysical context. Provided that dust grains are formed from the condensation of metals, we expect that the covering fractions and spatial distributions of neutral hydrogen gas, metals, and dust are related to some extent. It is extremely unlikely that dust exists in empty space or only ionized gas but not in neutral hydrogen gas, such that the dust covering fraction is completely independent of the H I covering fraction.

5.1.2. Dusty ISM/CGM Model

We now consider the second model, where dust and metals are exclusively confined to HI gas clumps. In the simplest scenario, the intraclump medium (ICM) is free of H I gas, dust, and metals. In this model, Ly α photons are scattered multiple times by the HI gas before escaping, leading to a longer path traveling through the ISM/CGM and higher probability of being attenuated by dust compared to the continuum photons. There are a few variations of the dusty ISM/CGM model that have different predictions depending on specific assumptions. Neufeld (1991) proposed a model where the dusty H I gas clumps are surrounded by an ICM that is optically thin to Ly α and has negligible dust content. In this model, the clumps are composed of optically thick HI gas with a high column density, and Ly α photons are scattered off of the clump surface without interacting with the shielded dust. Consequently, Ly α photons spend most of their time in the ICM bouncing between the clump surfaces, barely getting absorbed. In the meantime, continuum photons travel through the dusty clumps and are attenuated by the embedded dust. This model therefore predicts a positive correlation between EW_{Ly α} and E(B-V) (as Ly α photons are less attenuated by dust than continuum photons) and has been used to examine the "boosting" of $EW_{Lv\alpha}$ in $Ly\alpha$ emitters (LAEs) in high-redshift galaxies (Hansen & Oh 2006; Laursen et al. 2013; Duval et al. 2014), where the observed $EW_{Lv\alpha}$ is larger than what is theoretically expected.

However, previous observations showing an anticorrelation between $\mathrm{EW}_{\mathrm{Ly}\alpha}$ and E(B-V) (e.g., Shapley et al. 2003; Pentericci et al. 2007; Steidel et al. 2011; Du et al. 2018; Marchi et al. 2019) are in conflict with the Neufeld (1991) model. Furthermore, radiative transfer simulations have suggested that the Neufeld (1991) model requires weak to no outflows and a high density contrast between clumps and the ICM (Laursen et al. 2013; Duval et al. 2014), which do not appear to be realistic for the majority of galaxies at $z \gtrsim 2$.

These discrepancies motivate us to seek alternative dusty ISM/CGM models. One possibility is that the clumpiness of the ISM/CGM has low contrast, such that the ICM is also optically thick to Ly α photons (but not as high density as the gas clumps) and has a nonnegligible dust content (the "lowcontrast" regime in Duval et al. 2014). In this scenario, Ly α photons cannot escape without scattering in the ISM/CGM because of the optically thick ICM. Hence, even if Ly α photons are still scattered at the clump surfaces and remain unaffected by the dust embedded within, the Ly α flux can be more attenuated than the UV continuum flux because of the longer path $Ly\alpha$ photons take, on average (due to resonant scattering), through the ICM compared to continuum photons before escaping. We can therefore observe a negative correlation between $EW_{Ly\alpha}$ and E(B-V) as long as the cumulative E(B-V) in the ICM at the point of escape for $Ly\alpha$ photons is larger than the E(B-V) in the H I clumps. Another possibility is that the Ly α photons are in fact capable of penetrating the gas clumps and being absorbed by the embedded dust. This scenario requires the clumps to have a small velocity offset from the galaxy's systemic velocity, either in random motions or induced by stellar feedback, such that the Ly α photons are out of resonance with the HI gas clumps

(Hansen & Oh 2006; Laursen et al. 2013). The requirement of neutral clump motion is not difficult to fulfill at $z\sim2$, given the ubiquitously observed outflows in star-forming galaxies (Shapley et al. 2003; Steidel et al. 2004; Du et al. 2018). A scenario in which Ly α penetrates dusty clumps also leads to the differential attenuation between Ly α and the continuum photons and predicts a negative correlation between EW_{Ly α} and E(B-V) regardless of the dust content in the ICM.

Our results in Section 4 clearly agree more with a clumpy (and dusty) ISM/CGM model. Specifically, (1) EW_{LIS} and E(B-V) show the strongest correlation among the three correlations we have examined, indicating that the covering fractions of HI, dust, and metals are tightly connected. This piece of observational evidence suggests the possibility of HI, dust, and metals being cospatial, which is consistent with the dusty ISM/CGM model where dust and metals reside in the H I gas clumps. (2) On average, $EW_{Ly\alpha}$ and E(B-V) exhibit a negative correlation, consistent with Ly α photons within the region covered by the spectroscopic slit experiencing more attenuation than the continuum photons because of their longer paths through a dusty medium before escaping. An alternative explanation is that more Ly α photons are scattered out of the spectroscopic slit (while continuum photons remain unaffected) in galaxies with higher E(B-V), which typically also have a higher H_I covering fraction (Reddy et al. 2016). Either scenario described above requires the neutral hydrogen clumps to contain dust in order to explain the observed $EW_{Lv\alpha}$ versus E(B-V) trend. (3) Although the observed anticorrelation between EW_{Lv α} and E(B-V) indicates that the Neufeld (1991) scenario does not apply to the vast majority of the galaxies in our sample, we do observe a few outliers in the EW_{Ly α} versus E(B-V) relation (AEGIS-36451, COSMOS-2672, COSMOS-3974, COSMOS-6963, and COSMOS-26073). These galaxies are characterized by both relatively high global E(B-V) and prominent Ly α emission, and objects with similar E(B-V) and Ly α properties have been reported by previous studies (Hagen et al. 2014; Trainor et al. 2016). Interestingly, the presence of such outliers may indeed point to "boosted" Ly α emission in these galaxies (Neufeld 1991). For these outliers, the Ly α photons are perhaps less attenuated than the continuum photons if they are simply scattered off of the surfaces of high column density neutral clumps and consequently become insensitive to the dust embedded within the clumps. In short, while the Neufeld (1991) model cannot explain the overall EW_{Ly α} versus E (B-V) trend we observe, it may be applicable to the handful of "unusual" galaxies with both large $EW_{Ly\alpha}$ and high E (B-V). All of the results listed above are in support of the dusty ISM/CGM model, where dust and metals are located within neutral hydrogen gas clumps. While beyond the scope of this work, we note that our data allow variation in the dustto-metals ratio, which partially contributes to the apparent intrinsic scatter in the EW_{LIS} versus E(B-V) relation. Such variation has been shown from both observational and theoretical standpoints at low redshift (e.g., Chiang et al. 2018; Li et al. 2019) and may result from a large range of galactocentric radii where the LIS absorption takes place.

It is unfortunately impossible for us to determine the exact dust content in the ICM (e.g., dust-free or nonnegligible dust) using the current LRIS-ISM data. Predicted observables (such as the emergent Ly α profile and the expected strength or slope of the EW_{Ly α} versus E(B-V) relation) are needed to test the

hypotheses and distinguish these cases. Future simulations studying the propagation of $\text{Ly}\alpha$ photons through the clumpy, dusty ISM/CGM with different density contrasts between clumps and the ICM will provide key insights into this question. We further attribute the ICM dust content partially to the observed scatter in the $\text{EW}_{\text{Ly}\alpha}$ versus E(B-V) relation. It is possible that the ICM dust varies on a galaxy-by-galaxy basis, depending on the detailed star formation histories and stellar feedback of individual galaxies. We defer the discussion of the intrinsic scatter in the correlations to Section 5.2.

5.2. Intrinsic Scatter

Although statistically significant, the correlations among $\mathrm{EW}_{\mathrm{Ly}\alpha}$, $\mathrm{EW}_{\mathrm{LIS}}$, and E(B-V) are all subject to nonnegligible scatter introduced by different physical processes. To further investigate the origin of the intrinsic scatter in these relations, we test whether the observed galaxy-to-galaxy variation is correlated with any of the key galaxy properties under consideration.

5.2.1. Scatter Introduced by Metallicity

Using EW_{LIS} as a tracer of the H I covering fraction is based on several assumptions, which individually can introduce uncertainties into the observed EW_{LIS} versus $EW_{Ly\alpha}$ relation. Metal absorption in the spectra of galaxies is often used as a proxy for the neutral hydrogen content of the ISM. As the LIS lines are saturated in the LRIS spectra analyzed in this work, EW_{LIS} is not sensitive to the metal column density but rather the metal covering fraction. On the other hand, $EW_{Ly\alpha}$ is a probe of the H I covering fraction. Although the metal covering fraction can be used as a proxy for the H I covering fraction, the former is found, on average, to be systematically smaller than the latter (Reddy et al. 2016; Gazagnes et al. 2018). The ratio between the two can vary on an individual basis, as described below.

To further explore whether the metal-to-HI covering fraction ratio is a potential source of scatter, we examine the role of metallicity in the EW_{LIS} versus $EW_{Ly\alpha}$ relation. As demonstrated in Gazagnes et al. (2018) using Si II as a proxy for EW_{LIS}, one reason why the covering fraction of metals is correlated with but not equal to the H I covering fraction is that the metals are not fully mixed with the neutral hydrogen gas. These authors suggested that there are metal-enriched "pockets" residing in the HI gas. Furthermore, in lower-metallicity galaxies, the metal-to-HI covering fraction ratio is lower because there is less metal-rich gas and therefore fewer highdensity metal regions to absorb the background continuum.8 Accordingly, at fixed $EW_{Ly\alpha}$ (or approximately fixed H I covering fraction), we will observe lower-metallicity objects having smaller metal covering fractions, translating into weaker LIS absorption lines (lower EW_{LIS}) at fixed EW_{Ly α}. Simulations such as that presented in Mauerhofer et al. (2021) will be helpful for testing this scenario.

In the top and middle panels of Figure 5, we show measurements from individual galaxies (top) and composite

Although Gazagnes et al. (2018) showed that the covering fraction ratio between H I and Si II has a weak dependence on metallicity, the deduced relationship is only marginally more significant than that assuming that the covering fraction of H I solely depends on the Si II covering fraction. Therefore, it is still reasonable to assume that the covering fractions of H I and metals are closely correlated, although additional scatter can be introduced by different chemical abundance patterns when using specific metal-line probes.

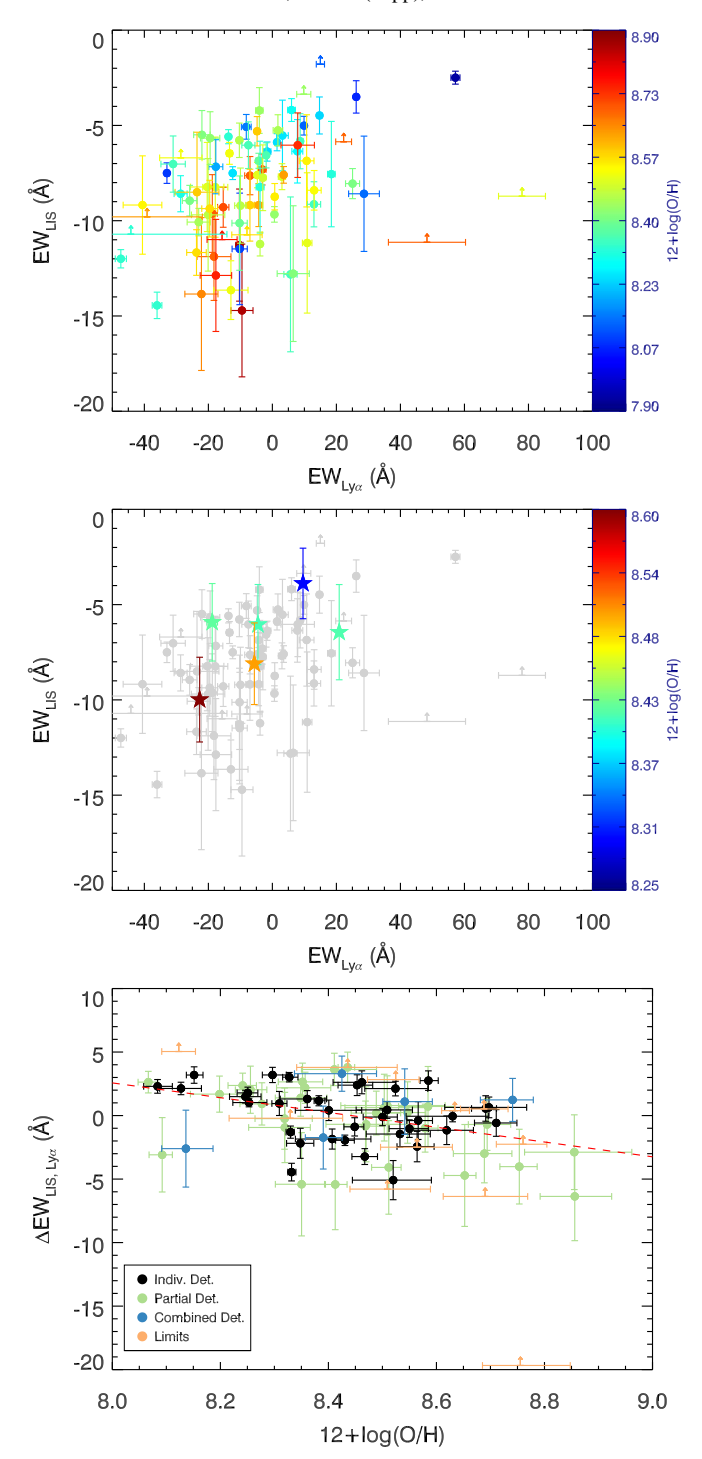


Figure 5. The EW_{LIS} vs. EW_{Lyα} relation as a function of metallicity. Top: EW_{LIS} vs. EW_{Lyα} for 82 objects with individual metallicity measurements. The data points are color coded by metallicity. The 1σ error bar is plotted for the LIS detections, while a 3σ limit is shown as an upward-pointing arrow for the LIS nondetections. Middle: EW_{LIS} vs. EW_{Lyα} for composite spectra created using 82 objects with individual metallicity measurements. The stacks were constructed by dividing 82 galaxies first into three bins in EW_{Lyα} and then into higher and lower halves in EW_{LIS} in each EW_{Lyα} bin. The median metallicity in each stack is shown. The individual measurements of all 157 LRIS-ISM galaxies are plotted as gray points for comparison. Bottom: residual EW_{LIS} at a given EW_{Lyα} vs. metallicity. The residual EW_{LIS} was calculated by taking the difference of the measured EW_{LIS} and the expected value at its EW_{Lyα}, indicated by the mean EW_{LIS} vs. EW_{Lyα} relation in Section 4. The red dashed line denotes the best-fit linear regression.

spectra (middle), color coded by metallicity, in the $EW_{Ly\alpha}$ versus EW_{LIS} parameter space. Metallicity for individual objects was determined based on $O32 \equiv [O \: III] \: \lambda 5007/[O \: II] \: \lambda \lambda 3727$, 3729 and other indicators when available, such as $O3 \equiv [O \: III] \: \lambda 5007/H\beta$ and $Ne3O2 \equiv [Ne \: III] \: \lambda 3869/[O \: II] \: \lambda \lambda 3727$, 3729, as described in Sanders et al. (2021). Such metallicity measurements make use of all available rest-optical emission lines from α elements (e.g., O, Ne). Using other common metallicity indicators, such as $[N \: II] \: \lambda 6584/H\alpha$ and $O3N2 \equiv ([O \: III] \: \lambda 5007/H\beta)/([N \: II] \: \lambda 6584/H\alpha)$ (Pettini & Pagel 2004), yields the same qualitative trends presented below.

To obtain robust metallicity measurements, we required spectral coverage and an $S/N \ge 3$ detection of at least [O II] and [O III] and of H β and/or [Ne III] when applicable. As a result, 82 out of 157 objects (52%) have a valid metallicity estimate. We note that these 82 objects are representative of the full LRIS-ISM sample in galaxy properties, except that they all have redshifts above z = 2.0857 to allow coverage of [O II] in the J band. We used the same 82 objects to create composite spectra, first dividing the subsample into three bins in $EW_{Lv\alpha}$ and then into higher and lower halves in EW_{LIS} within each $EW_{Lv\alpha}$ bin (six bins in total). Composite science and error spectra were created following the methodology of Du et al. (2018). In short, we performed median stacking after interpolating individual galaxy spectra in each bin onto the same grid in wavelength. The corresponding composite error spectra were constructed by calculating the standard deviation of 100 fake median stacks at each wavelength, where the fake stacks were created by bootstrap-resampling the objects in each bin and perturbing individual galaxy spectra in the bootstrapped sample by their associated error spectra. The measurements of $EW_{Ly\alpha}$ and EW_{LIS} in the composite spectra followed the descriptions in Section 3, and we plot the median metallicity in each composite. Both individual and composite spectra suggest that at fixed $EW_{L\nu\alpha}$, LIS features are stronger in higher-metallicity objects or stacks.

The bottom panel of Figure 5 further supports the claim that metallicity plays a key role in the observed EW_{Ly\alpha} versus EW_{LIS} relationship. The residual EW_{LIS}, Δ EW_{LIS,Ly\alpha}, was calculated by subtracting from each measured EW_{LIS} the expected EW_{LIS} based on the galaxy's EW_{Ly\alpha}, as defined by the mean EW_{Ly\alpha} versus EW_{LIS} relation in Table 2. In the bottom panel, we observe that Δ EW_{LIS,Ly\alpha} decreases with increasing metallicity. This trend is statistically significant (Spearman's $\rho = -0.314$; the probability of a null hypothesis is 0.0048) and again indicates that the LIS lines become stronger, at fixed EW_{Ly\alpha}, with increasing metallicity. This finding not only supports the proposed physical scenario of inhomogeneous metal mixing but also highlights one key source of the scatter in the EW_{Ly\alpha} versus EW_{LIS} relation: metallicity.

Our results here can be compared with those presented in Trainor et al. (2019), who found that $EW_{Ly\alpha}$ corresponds to higher O3 at fixed EW_{LIS} . Given that O3 is anticorrelated with metallicity in the regimes probed in both studies, our findings are in qualitative agreement with those in Trainor et al. (2019). In our work, we interpret the results as a metallicity variance across the $EW_{Ly\alpha}$ versus EW_{LIS} parameter space, which contributes scatter to the observed relation.

In summary, while interstellar metal absorption lines have proven to be a reasonable tracer of H I gas, intrinsic scatter in the

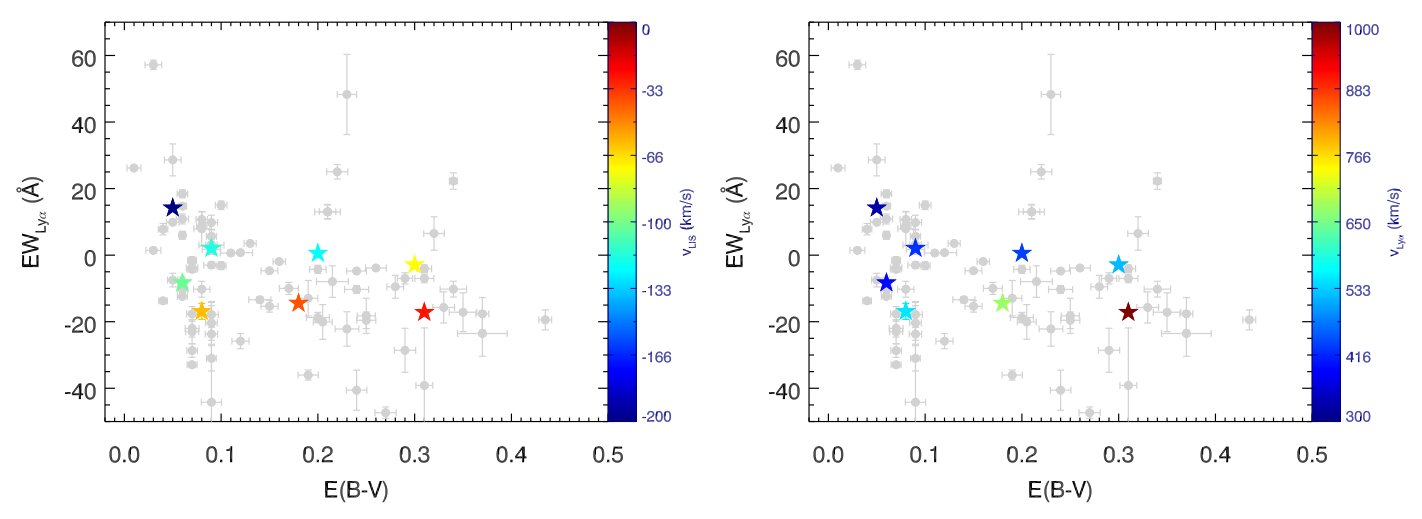


Figure 6. $EW_{Ly\alpha}$ vs. E(B-V) for composite spectra color coded by the LIS (left; v_{LIS}) and $Ly\alpha$ (right; $v_{Ly\alpha}$) velocity shifts. The composite was constructed by dividing all 157 galaxies first into four bins of E(B-V) and then into higher and lower halves in $EW_{Ly\alpha}$ in each E(B-V) quartile. The individual measurements are plotted as gray points for comparison. The velocity shifts were calculated based on the average centroid velocity of Si II λ 1260, O I λ 1302+Si II λ 1304, and C II λ 1334 for v_{LIS} and the centroid of the $Ly\alpha$ emission peak for $v_{Ly\alpha}$.

 EW_{LJS} versus $EW_{Ly\alpha}$ relation inevitably arises from the object-to-object variation in the metal–to–H I covering fraction ratio. Here we connect this ratio with gas-phase metallicity, which is determined by the star formation histories, stellar populations, galaxy age, and galactic-scale gas flows (e.g., Tremonti et al. 2004; Sanders et al. 2021). Other factors related to metallicity, such as nebular ionization, may further contribute to the intrinsic scatter in the $EW_{Ly\alpha}$ versus EW_{LIS} relation, as explored in previous work (Trainor et al. 2019).

5.2.2. Scatter Introduced by Outflow Kinematics

Galactic-scale outflows are ubiquitously observed at $z \gtrsim 2$ (Pettini et al. 2002; Shapley et al. 2003; Steidel et al. 2010) and have a significant impact on the radiative transfer of Ly α photons through the neutral ISM/CGM. As a result, outflow kinematics can modulate the emergent Ly α profile and, accordingly, EW_{Ly α}.

As detailed in Section 3.2.1, the Ly α feature in the LRIS-ISM spectra is observed to have various profile morphologies. Previous studies have examined how outflow kinematics can alter the observed Ly α profile. For example, Verhamme et al. (2006) used a 3D Ly α radiation transfer code to study the emergent Ly α line profiles in galaxy environments with different HI densities, dust distributions, and velocity fields. Additionally, Steidel et al. (2010) proposed an analytical model of the outflowing ISM/CGM to explain the variation in the observed Ly α emission profile. Their results suggest that the HI covering fraction near the galaxy's systemic velocity ($v \simeq 0$) is responsible for the observed redshifted peak of Lya; the higher the HI covering fraction, the more absorption at $v \simeq 0$, pushing the observed Ly α peak toward a redder wavelength and reducing the overall $EW_{Ly\alpha}$. In terms of a physical picture, redder (and typically weaker) Ly α emission signals the fact that only photons emitted or scattered by the materials on the far side of the galaxy that have a redshifted velocity large enough to make Ly α photons out of resonance with the foreground HI can escape in the observer's direction.

Given that outflow kinematics may be one factor modulating $\mathrm{EW}_{\mathrm{Ly}\alpha}$, we examine how $\mathrm{Ly}\alpha$ and LIS velocity shifts ($\nu_{\mathrm{Ly}\alpha}$ and ν_{LIS} , respectively) affect the $\mathrm{EW}_{\mathrm{Ly}\alpha}$ versus E(B-V) relation. The velocity shift of a line is defined as $\nu = (\lambda_{\mathrm{obs}} - \lambda_{\mathrm{rest}})/\lambda_{\mathrm{rest}} \times c$,

where $\lambda_{\rm obs}$ and $\lambda_{\rm rest}$ are, respectively, the observed and rest-frame wavelengths of the spectral feature. Figure 6 shows composite spectra, color coded by $v_{\rm LIS}$ (left) and $v_{\rm Ly\alpha}$ (right), in the EW_{Ly\alpha} versus E(B-V) plane. The composites make use of all 157 objects in the LRIS-ISM sample and were binned first according E(B-V) and then divided into higher and lower halves in EW_{Ly\alpha} in each E(B-V) quartile. The $v_{\rm LIS}$ was estimated as the average centroid velocity of Si II λ 1260, O I λ 1302+Si II λ 1304, and C II λ 1334, where the centroid of the respective lines was returned by MPFIT (see Section 3.2.2). We measured $v_{\rm Ly\alpha}$ based on the Ly\alpha emission peak, which was fit with a Gaussian profile over the wavelength range bracketed by the blue and red bases of the Ly\alpha emission profile. We note that, while weak, the Ly\alpha emission peak is still discernible in stacks categorized as "absorption" in Ly\alpha morphology.

We find that at fixed E(B-V), Ly α is stronger in galaxies with larger LIS blueshifts and smaller Ly α redshifts. This result not only identifies outflow kinematics as a contributor to the observed scatter in the $\mathrm{EW}_{\mathrm{Ly}\alpha}$ versus $\mathit{E}(\mathit{B}-\mathit{V})$ relation but also highlights conditions favorable for Ly α photon escape. The centroid velocity of the LIS lines describes the bulk movement of the neutral, metal-enriched gas. Therefore, larger LIS blueshifts in general correspond to higher outflow velocities, with which outflows may clear out channels through the ISM/CGM efficiently, reducing the covering fraction of H I gas and allowing for the escape of Ly α photons. On the other hand, the higher the bulk outflow velocities, the smaller the fraction of H I gas that is expected to be moving at $v \simeq 0$, resulting in less redshifted and stronger Ly α emission. Our findings agree with the predictions of the Steidel et al. (2010) model and demonstrate that outflow kinematics, as determined by star formation activities, can introduce considerable scatter in the observed EW_{Ly α} versus E(B-V) relation.

5.2.3. Other Physical Origins of Scatter

Aside from the key observables investigated in the previous sections, such as metallicity, $v_{\rm Ly\alpha}$, and $v_{\rm LIS}$, other factors or physical processes may have contributed to the observed scatter in the correlations involving EW_{Ly\alpha}, EW_{LIS}, and E(B-V). In

this section, we briefly discuss the other possible origins of scatter in an astrophysical context.

Ly α production. In Section 4, the overall trend between EW_{Ly α} and EW_{LIS} highlights the importance of resonant scattering of Ly α photons by H I gas. It is worth mentioning that the observed $Ly\alpha$ EW depends on not only the escape but also the production of Ly α photons. Although this effect impacts all objects regardless of their $EW_{Ly\alpha}$, it is especially prominent in LAEs (rest-frame $EW_{Lv\alpha} \ge 20 \text{ A}$), where the hard ionizing spectrum associated with metal-poor star formation boosts the intrinsic Ly α production as well as lowers the H I covering fraction by ionizing the H I gas in the ISM (Erb et al. 2016; Reddy et al. 2016; Trainor et al. 2016). While we expect the variation in Ly α production to play a relatively small role in the majority of the galaxies in the LRIS-ISM sample (the median $EW_{Ly\alpha}$ is -6.0 Å), there are in fact 15 galaxies with EW_{Ly α} \geqslant 20 Å. Hence, the \sim 10% LAEs in the sample may have introduced some scatter in the observed relations involving $EW_{Lv\alpha}$ due to their higher-than-average $Ly\alpha$ production efficiency.

Slit loss. Slit spectroscopy is typically used for observing the compact continuum-emitting regions of high-redshift star-forming galaxies. At $z \sim 2.3$, the median redshift of the LRIS-ISM sample, the slit width of 1"2 corresponds to a physical size of \sim 10 kpc. As shown by previous work (Steidel et al. 2010; Matsuda et al. 2012), the cool-phase CGM, where low ions are used to trace H I gas, has a physical scale ≥ 100 kpc at $z \sim 2-3$. Accordingly, slit spectra can only capture the CGM at relatively small galactocentric radii, and the inferred galaxy properties and measured line strengths are largely "local" rather than "global." In particular, multiple studies have reported extended Ly α halos (\sim 80–100 kpc) surrounding star-forming galaxies at $z \sim 2-3$ (Steidel et al. 2011; Matsuda et al. 2012). If the slit spectra can only collect Ly α photons emitted/ escaping from the innermost 10 kpc, the observed $EW_{L_{VQ}}$ may not be an accurate proxy for the actual $EW_{Lv\alpha}$ we would observe with slitless spectroscopy.

To test the effect slit loss has on the variation of $EW_{Ly\alpha}$, we obtained the continuum size of the MOSDEF-LRIS galaxies in the HST/F160W filter, drawn from the van der Wel et al. (2014) catalog. Preliminary results suggest that $\Delta EW_{Lv\alpha,E(B-V)}$ (i.e., the "residual" $EW_{Lv\alpha}$ at fixed E(B-V) as predicted by the mean $EW_{L_{NO}}$ versus E(B-V) relation) is not correlated with either the galaxy physical size (in kiloparsecs) or the ratio of the slit width and the galaxy angular size in the H band. We caution that our result is inconclusive in determining the contribution of slit loss to the scatter in the EW_{Lv α} versus (B-V) relation, as the galaxy size indicated by stellar continuum emission is different from that indicated by Ly α emission. Hence, narrowband imaging and integral field unit (IFU) observations (e.g., the Keck Cosmic Web Imager) are needed to (1) characterize the physical scale of the Ly α halo in these galaxies and quantify the effect of slit loss on the measurement of $EW_{Ly\alpha}$ and (2) determine whether the observed anticorrelation between EW_{Lv α} versus E(B-V) originates from the preferential dust attenuation of Ly α photons relative to continuum photons or is simply an effect of the scattering of Ly α photons by HI out of the spectroscopic slit.

6. Summary

Rest-UV spectra provide unique information on the structure of the ISM/CGM in star-forming galaxies. The LIS absorption features are commonly used to probe the neutral CGM. Along with Ly α and other key galaxy properties, such as dust extinction, the geometry and physical distributions of H I gas,

metals, and dust can be inferred. Using deep rest-UV LRIS spectra, we obtained individual measurements of EW_{Lyα}, EW_{LIS}, and E(B-V) for a statistical sample of 157 objects. Rest-optical MOSFIRE spectra provide additional data for each object, including the systemic redshift and gas-phase metallicity. We characterize the tightness of the mutual correlations among EW_{Lyα}, EW_{LIS}, and E(B-V) using statistical analysis and identify the factors that contribute to the intrinsic scatter in the relations. Below, we summarize our main findings.

- 1. $EW_{Ly\alpha}$, EW_{LIS} , and E(B-V) are intercorrelated. EW_{LIS} and E(B-V) display a positive correlation, and galaxies with stronger EW_{LIS} or larger E(B-V), on average, have smaller $EW_{Ly\alpha}$. This result agrees with those from previous studies using measurements from composite galaxy spectra. This finding supports a picture where $Ly\alpha$ photons are resonantly scattered by the clumpy H I gas, being absorbed by dust as they travel through the ISM/CGM, and escape the ISM/CGM through channels with low H I covering fractions and/or column densities.
- 2. Using statistical analysis, we find that all three mutual correlations among $\mathrm{EW}_{\mathrm{Ly}\alpha}$, $\mathrm{EW}_{\mathrm{LIS}}$, and E(B-V) are statistically significant. The strongest relation is between $\mathrm{EW}_{\mathrm{LIS}}$ and E(B-V), while the $\mathrm{EW}_{\mathrm{Ly}\alpha}$ versus $\mathrm{EW}_{\mathrm{LIS}}$ relation is the weakest. The ordering of correlation strengths does not depend on the inclusion of $\mathrm{EW}_{\mathrm{LIS}}$ nondetections.
- 3. The fact that the EW_{LIS} versus E(B-V) relation appears to be the most fundamental one among the three correlations highlights the physical connections between dust and metalenriched H I gas, suggesting that they are likely to be cospatial. The observed correlation between EW_{Lv α} and E(B-V)suggests either the preferential dust attenuation of Ly α photons compared to continuum photons or a larger fraction of Ly α photons being scattered out of the slit in galaxies with a higher E(B-V) and H I covering fraction. Finally, part of the apparent scatter in the $EW_{Ly\alpha}$ versus EW_{LIS} relation can be explained by the difference in the metal-to-HI covering fraction ratio that is driven by variations in metallicity (as traced by rest-optical nebular emission line ratios in our framework) on an individual basis. The metal covering fraction, which determines the strength of the saturated LIS lines, does not directly probe the covering fraction of HI gas that modulates $EW_{L\nu\alpha}$. We have further identified outflow kinematics and the amount of dust in the ICM as two factors that can contribute to the scatter in the EW_{Lv α} versus E(B-V)relation.
- 4. In addition to metallicity and outflow kinematics, we have qualitatively determined other possible origins of the scatter in the mutual correlations involving $\mathrm{EW}_{\mathrm{Ly}\alpha}$, $\mathrm{EW}_{\mathrm{LIS}}$, and E(B-V). These include (i) $\mathrm{Ly}\alpha$ production efficiency, which is particularly important for LAEs (Reddy et al. 2016), where the emergent $\mathrm{Ly}\alpha$ flux is not only determined by the escape but also the production of $\mathrm{Ly}\alpha$ photons, and (ii) slit loss, which can potentially impact the global measurements of $\mathrm{EW}_{\mathrm{Ly}\alpha}$, $\mathrm{EW}_{\mathrm{LIS}}$, and E(B-V) due to finite slit width.
- 5. We have reviewed two previously proposed CGM models that consider different spatial distributions of H I gas, dust, and metals. Based on the strongest correlation observed between $\mathrm{EW}_{\mathrm{LIS}}$ and E(B-V) and the existence of objects with prominent $\mathrm{Ly}\alpha$ emission and large E(B-V), our data prefer the dusty ISM/CGM model where dust resides in the H I gas clumps instead of being distributed in a uniform foreground screen. The uniform dust screen model is further disfavored

because it is physically unlikely and predicts no dependence between $EW_{L_{VO}}$ and E(B-V), which contradicts our findings.

Confirming the detailed ISM/CGM structure in typical starforming galaxies requires not only high-quality multidimensional data but also simulations that incorporate radiative transfer of Ly α and stellar feedback to compare with observational constraints. For example, narrowband images focused near Ly α yield valuable information on the size of the Ly α halo and the extended CGM, providing calibrations and correction factors for the observed line EWs in slit spectroscopy. The IFU spectroscopic maps will provide additional insights into the spatial variation of galaxy properties and line strengths, revealing the small-scale physical processes that lead to the intrinsic scatter in the observed correlations and informing CGM models based on the spatially resolved gas and dust properties (e.g., Bridge et al. 2018). Finally, simulations with prescriptions of stellar feedback and radiative transfer can test different CGM models and predict the expected $EW_{Ly\alpha}$ and E(B-V) relation based on different relative spatial distributions of HI gas and dust. A robust understanding of the structure of the CGM will enlighten us on topics such as (1) the escape fractions of Ly α and LyC photons and (2) the nature of the relations among neutral hydrogen gas, dust, and metals. Further observational data and analytical models that directly address these questions are essential for making progress toward that end.

We thank the referee, Ryan Trainor, for a thorough and constructive report that improved the paper. We acknowledge support from NSF AAG grants AST1312780, 1312547, 1312764, and 1313171; grant AR13907 from the Space Telescope Science Institute; and grant NNX16AF54G from the NASA ADAP program. We also acknowledge a NASA contract supporting the "WFIRST Extragalactic Potential Observations (EXPO) Science Investigation Team" (15-WFIRST15-0004), administered by the GSFC. X.D. and B.M. further acknowledge support from the NASA MUREP Institutional Research Opportunity (MIRO) through grant NNX15AP99A, as well as the MUREP Aerospace Academy (MAA) through grant 80NSSC19M0099. We are grateful to the 3D-HST team for providing ancillary data on galaxy properties. We wish to extend special thanks to those of Hawaiian ancestry on whose sacred mountain we are privileged to be guests. Without their generous hospitality, most of the observations presented herein would not have been possible.

ORCID iDs

References

```
Asplund, M., Grevesse, N., Sauval, A. J., & Scott, P. 2009, ARA&A, 47, 481 Azadi, M., Coil, A., Aird, J., et al. 2018, ApJ, 866, 63 Azadi, M., Coil, A. L., Aird, J., et al. 2017, ApJ, 835, 27 Berry, M., Gawiser, E., Guaita, L., et al. 2012, ApJ, 749, 4 Brammer, G. B., van Dokkum, P. G., Franx, M., et al. 2012, ApJS, 200, 13 Bridge, J. S., Hayes, M., Melinder, J., et al. 2018, ApJ, 852, 9
```

```
Bruzual, G., & Charlot, S. 2003, MNRAS, 344, 1000
Calzetti, D., Armus, L., Bohlin, R. C., et al. 2000, ApJ, 533, 682
Cardelli, J. A., Clayton, G. C., & Mathis, J. S. 1989, ApJ, 345, 245
Chabrier, G. 2003, PASP, 115, 763
Chiang, I.-D., Sandstrom, K. M., Chastenet, J., et al. 2018, ApJ, 865, 117
Coil, A. L., Aird, J., Reddy, N., et al. 2015, ApJ, 801, 35
Du, X., Shapley, A. E., Martin, C. L., & Coil, A. L. 2016, ApJ, 829, 64
Du, X., Shapley, A. E., Reddy, N. A., et al. 2018, ApJ, 860, 75
Duval, F., Schaerer, D., Östlin, G., & Laursen, P. 2014, A&A, 562, A52
Erb, D. K., Pettini, M., Shapley, A. E., et al. 2010, ApJ, 719, 1168
Erb, D. K., Pettini, M., Steidel, C. C., et al. 2016, ApJ, 830, 52
Feigelson, E. D., & Nelson, P. I. 1985, ApJ, 293, 192
Gazagnes, S., Chisholm, J., Schaerer, D., et al. 2018, A&A, 616, A29
Grogin, N. A., Kocevski, D. D., Faber, S. M., et al. 2011, ApJS, 197, 35
Hagen, A., Ciardullo, R., Gronwall, C., et al. 2014, ApJ, 786, 59
Hansen, M., & Oh, S. P. 2006, MNRAS, 367, 979
Isobe, T., & Feigelson, E. D. 1990, BAAS, 22, 917
Isobe, T., Feigelson, E. D., & Nelson, P. I. 1986, ApJ, 306, 490
Jaskot, A. E., Dowd, T., Oey, M. S., Scarlata, C., & McKinney, J. 2019, ApJ,
Jones, T., Stark, D. P., & Ellis, R. S. 2012, ApJ, 751, 51
Kelly, B. C. 2007, ApJ, 665, 1489
Koekemoer, A. M., Faber, S. M., Ferguson, H. C., et al. 2011, ApJS, 197, 36
Kornei, K. A., Shapley, A. E., Erb, D. K., et al. 2010, ApJ, 711, 693
Kriek, M., Shapley, A. E., Reddy, N. A., et al. 2015, ApJS, 218, 15
Laursen, P., Duval, F., & Östlin, G. 2013, ApJ, 766, 124
Lavalley, M., Isobe, T., & Feigelson, E. 1992, in ASP Conf. Ser. 25,
   Astronomical Data Analysis Software and Systems I, ed. D. M. Worrall,
  C. Biemesderfer, & J. Barnes (San Francisco, CA: ASP), 245
Leung, G. C. K., Coil, A. L., Aird, J., et al. 2019, ApJ, 886, 11
Li, Q., Narayanan, D., & Davé, R. 2019, MNRAS, 490, 1425
Marchi, F., Pentericci, L., Guaita, L., et al. 2019, A&A, 631, A19
Markwardt, C. B. 2009, in ASP Conf. Ser. 411, Astronomical Data Analysis
   Software and Systems XVIII, ed. D. A. Bohlender, D. Durand, & P. Dowler
  (San Francisco, CA: ASP), 251
Matsuda, Y., Yamada, T., Hayashino, T., et al. 2012, MNRAS, 425, 878
Mauerhofer, V., Verhamme, A., Blaizot, J., et al. 2021, A&A, 646, A80
McLean, I. S., Steidel, C. C., Epps, H. W., et al. 2012, Proc. SPIE, 8446, 84460J
Neufeld, D. A. 1991, ApJL, 370, L85
Oke, J. B., Cohen, J. G., Carr, M., et al. 1995, PASP, 107, 375
Pahl, A. J., Shapley, A., Faisst, A. L., et al. 2020, MNRAS, 493, 3194
Pentericci, L., Grazian, A., Fontana, A., et al. 2007, A&A, 471, 433
Pentericci, L., Grazian, A., Fontana, A., et al. 2009, A&A, 494, 553
Pettini, M., & Pagel, B. E. J. 2004, MNRAS, 348, L59
Pettini, M., Rix, S. A., Steidel, C. C., et al. 2002, ApJ, 569, 742
Pettini, M., Shapley, A. E., Steidel, C. C., et al. 2001, ApJ, 554, 981
Reddy, N. A., Oesch, P. A., Bouwens, R. J., et al. 2018, ApJ, 853, 56
Reddy, N. A., Pettini, M., Steidel, C. C., et al. 2012, ApJ, 754, 25
Reddy, N. A., Steidel, C. C., Pettini, M., Bogosavljević, M., & Shapley, A. E.
  2016, ApJ, 828, 108
Rivera-Thorsen, T. E., Hayes, M., Östlin, G., et al. 2015, ApJ, 805, 14
Rix, S. A., Pettini, M., Leitherer, C., et al. 2004, ApJ, 615, 98
Sanders, R. L., Shapley, A. E., Jones, T., et al. 2021, ApJ, 914, 19
Shapley, A. E., Steidel, C. C., Adelberger, K. L., et al. 2001, ApJ, 562, 95
Shapley, A. E., Steidel, C. C., Pettini, M., & Adelberger, K. L. 2003, ApJ,
  588, 65
Shapley, A. E., Steidel, C. C., Pettini, M., Adelberger, K. L., & Erb, D. K.
  2006, ApJ, 651, 688
Shivaei, I., Reddy, N., Rieke, G., et al. 2020, ApJ, 899, 117
Shivaei, I., Reddy, N. A., Shapley, A. E., et al. 2015, ApJ, 815, 98
Skelton, R. E., Whitaker, K. E., Momcheva, I. G., et al. 2014, ApJS, 214, 24
Steidel, C. C., Bogosavljević, M., Shapley, A. E., et al. 2011, ApJ, 736, 160
Steidel, C. C., Bogosavljević, M., Shapley, A. E., et al. 2018, ApJ, 869, 123
Steidel, C. C., Erb, D. K., Shapley, A. E., et al. 2010, ApJ, 717, 289
Steidel, C. C., Rudie, G. C., Strom, A. L., et al. 2014, ApJ, 795, 165
Steidel, C. C., Shapley, A. E., Pettini, M., et al. 2004, ApJ, 604, 534
Strom, A. L., Steidel, C. C., Rudie, G. C., et al. 2017, ApJ, 836, 164
Topping, M. W., Shapley, A. E., Reddy, N. A., et al. 2020, MNRAS, 495, 4430
Trainor, R. F., Strom, A. L., Steidel, C. C., et al. 2019, ApJ, 887, 85
Trainor, R. F., Strom, A. L., Steidel, C. C., & Rudie, G. C. 2016, ApJ, 832, 171
Tremonti, C. A., Heckman, T. M., Kauffmann, G., et al. 2004, ApJ, 613, 898
Tumlinson, J., Peeples, M. S., & Werk, J. K. 2017, ARA&A, 55, 389
van der Wel, A., Franx, M., van Dokkum, P. G., et al. 2014, ApJ, 788, 28
Vasei, K., Siana, B., Shapley, A. E., et al. 2016, ApJ, 831, 38
Verhamme, A., Schaerer, D., & Maselli, A. 2006, A&A, 460, 397
Yang, H., Malhotra, S., Gronke, M., et al. 2017, ApJ, 844, 171
```